Predicting Personalised Therapeutic Combinations in Non-Small Cell Lung Cancer Using *In Silico* Modelling

Matthew A. Clarke[1^], Charlie George Barker[1^], Ashley Nicholls[2^], Matt P. Handler[1], Lisa Pickard[3], Amna Shah[4], David Walter[5], Etienne De Braekeleer[6], Udai Banerji[3], Jyoti Choudhary[3], Saif Ahmed[2], Ultan McDermott[4], Gregory J. Hannon[2*] and Jasmin Fisher[1*]

[1] UCL Cancer Institute, University College London, 72 Huntley Street, London, WC1E 6DD, UK
[2] Cancer Research UK Cambridge Institute, University of Cambridge, Cambridge, CB2 0RE, UK
[3] The Institute of Cancer Research, 123 Old Brompton Road, London, SW7 3RP, UK
[4] AstraZeneca, Oncology R&D, 1 Francis Crick Avenue, Cambridge, CB2 0AA, UK
[5] Cancer Research Horizons, Cambridge, CB2 0RE, UK
[6] AstraZeneca, Discovery Science R&D, 1 Francis Crick Avenue, Cambridge, CB2 0AA, UK

^These authors contributed equally to this work

*Correspondence should be addressed to Jasmin Fisher jasmin.fisher@ucl.ac.uk or Gregory Hannon greg.hannon@cruk.cam.ac.uk

Abstract

The disease burden from non-small cell lung cancer (NSCLC) adenocarcinoma is substantial, with around a million new cases diagnosed globally each year, and a 5-year survival rate of less than 20%. A lack of therapeutic options personalized to individual patient genetics, and the targeted therapies that exist quickly succumbing to resistance, leads to high variation in survival. Patient stratification combined with greater personalisation of therapies have the potential to improve outcomes, however, the wide variation in mutations found in NSCLC adenocarcinoma patients mean that experimentally determining suitable treatment combinations is time-consuming and expensive. Here we present an *in silico* model encompassing tumour intrinsic key oncogenic signalling pathways, including EGFR, AKT, JAK/STAT and WNT for efficiently predicting rational drug-drug and drug-radiotherapy combination therapies in NSCLC. Using this model, we simulate diverse genetic profiles and test over 10,000 therapeutic strategies to identify optimal strategies to overcome resistance mechanisms specific to genetic profiles and p53 status. Our *in silico* model reproduces drug additivity experiments, predicts radio-sensitising genes validated in a CRISPR screen and identifies 53BP1 as a potential drug target that improves the therapeutic window during radiotherapy, as well as potential to use ATM inhibitors to overcome p53 loss-of-function driven radiotherapy resistance. We further use the *in silico* model to identify a 19-gene signature to stratify patients most likely to benefit from radiotherapy and validated this using TCGA data. These results further demonstrate the utility of *in silico* mechanistic modelling and present a bespoke computational resource for large-scale screening of personalised therapies applied to NSCLC.

Introduction

Lung cancer is the leading cause of cancer-related deaths worldwide, resulting in an estimated 1.8 million deaths annually. Non-small cell lung cancer (NSCLC) adenocarcinoma accounts for ~85% of lung cancer cases and has a 5-year survival rate of 19%[1]. Treatment options have advanced substantially over the last 10 years, with new surgical approaches, chemotherapeutic drugs and better targeted radiotherapy, with patients now often treated with several of these in combination[1,2]. However, overall survival remains low[3], in part because current approaches do not account for the diversity of oncogenic mutations driving NSCLC[4]. Furthermore, in cases where targeted therapy is applicable, resistance is inevitable, with the majority of patients treated with first-generation EGFR inhibitors developing resistance after 6-9 months of treatment[1,5–7]. A lack of understanding of how tumour genetics affect response to therapy, and the mechanisms underlying resistance, limit our ability to rationally design treatments that pre-empt and overcome resistance, and personalise therapeutics to maximise individual patient outcomes[8].

Radiotherapy delivers a high dose of radiation to cancer cells to cause the rapid accumulation of double-stranded breaks (DSBs)[9,10]. If unrepaired, these DSBs trigger cell death[11], while healthy cells are better able to repair these breaks and survive. Radiotherapy has a significantly lower treatment-associated mortality than surgery[12], although the efficacy of surgery is higher than that of radiotherapy in terms of overall survival[13], owing in part to adaptation of the tumour and evolution of radio resistance-associated mutations[14]. Extending the benefits of radiotherapy to more patients and improving efficacy to reduce the chance of resistance emerging requires better understanding of how variation in treatment response is driven by differences in driver mutations. This will allow tailoring of radiotherapy to patient biology by combining it with radio-sensitising treatments.

Recent advances in modelling patient biology as executable computer programs are now beginning to uncover the principles underlying how the genetics of a cancer contributes to its behaviour and the potential mechanisms that give rise to phenotypes such as therapeutic resistance[15–21]. Here, we present a bespoke executable model of NSCLC adenocarcinoma oncogenic signalling that covers key pathways including the cell cycle, apoptosis cascade and DNA damage response (DDR). This model can mechanistically link oncogenic genetics and signalling, by representing biological processes as nodes within a qualitative network, with functions determining the activation of biological components[22]. The model is 'executed' by allowing nodes to interact with each other dynamically, such that the stable state of the network represents the overall cellular phenotype[23]. The model can be used to test combinations of mutations and inhibitors involving proteins that are not yet druggable, allowing identification of potential drug targets for future research and development. It can also be interrogated in greater depth than real systems as every variable and interaction in the model can be controlled individually, allowing for more complete exploration of the mechanisms underpinning observations. Moreover, this mechanistic understanding of how therapy interacts with the oncogenic mutations allows us to identify the genetic determinants of responses to therapy.

Here we use this *in silico* model to explore 136 possible radio-sensitising treatments across a panel of 7 cancer cell lines and explore the effect of specific mutations on treatment sensitivity. Once the model successfully recapitulates previously published sensitivities of different NSCLC adenocarcinoma cell lines to combination drug treatment and radiotherapy, we use the model

to screen ~66,000 combinations to find the optimal therapeutic strategy for a given genotype. We exploit the interpretable nature of our i*n silico* model to understand why these sensitivities occur and how specific mutations determine the NSCLC adenocarcinoma responses to therapy. We then perform *in silico* screens for perturbations that can sensitise cancer cells to radiotherapy while protecting healthy cells, as well as overcome p53-driven radiotherapy resistance. Overall, our platform is a powerful tool for understanding therapeutic responses to treatment in NSCLC. Harnessing the power of executable models will provide a more complete understanding of how genetics contributes to oncogenic signalling and enable therapy to be tailored to the genetics underlying the cancer, improving treatment outcomes for patients.

Results

An executable network map of KRAS-, EGFR- and MET- driven NSCLC adenocarcinoma

To understand the contributions of oncogenic mutations in NSCLC adenocarcinoma to drug and radiotherapy response, we built an executable qualitative network model using the BioModelAnalyzer (BMA) tool (https://biomodelanalyzer.org, see Methods) following the workflow outlined in Figure 1A. The model describes the core pathways covering the most common driver mutations in NSCLC patients[24], including EGFR, AKT, JAK/STAT and WNT pathways, as well as commonly overexpressed genes such as MYC and NRF2. We modelled how these mutations drive changes in cell cycle and apoptosis. To model radiotherapy responses, we include the DNA damage repair (DDR) pathways, homologous recombination (HR) and Non-Homologous End Joining (NHEJ).

An extensive literature survey of 171 research papers identified interactions between genes and proteins in NSCLC adenocarcinoma resulting in a model with 160 nodes and 360 edges describing activating regulatory relationships or inhibiting relationships between biological components (Supplementary Table S1). To provide context to these interactions, each node has a corresponding target function defining its activity (Shown in Figure 1B, Supplementary Table S1, S2 and S3). The value describing the activity of nodes is discrete and ranges between 4 levels (0 to 3). A level of 0 indicates loss-of-function and 3 indicates gain-of-function.

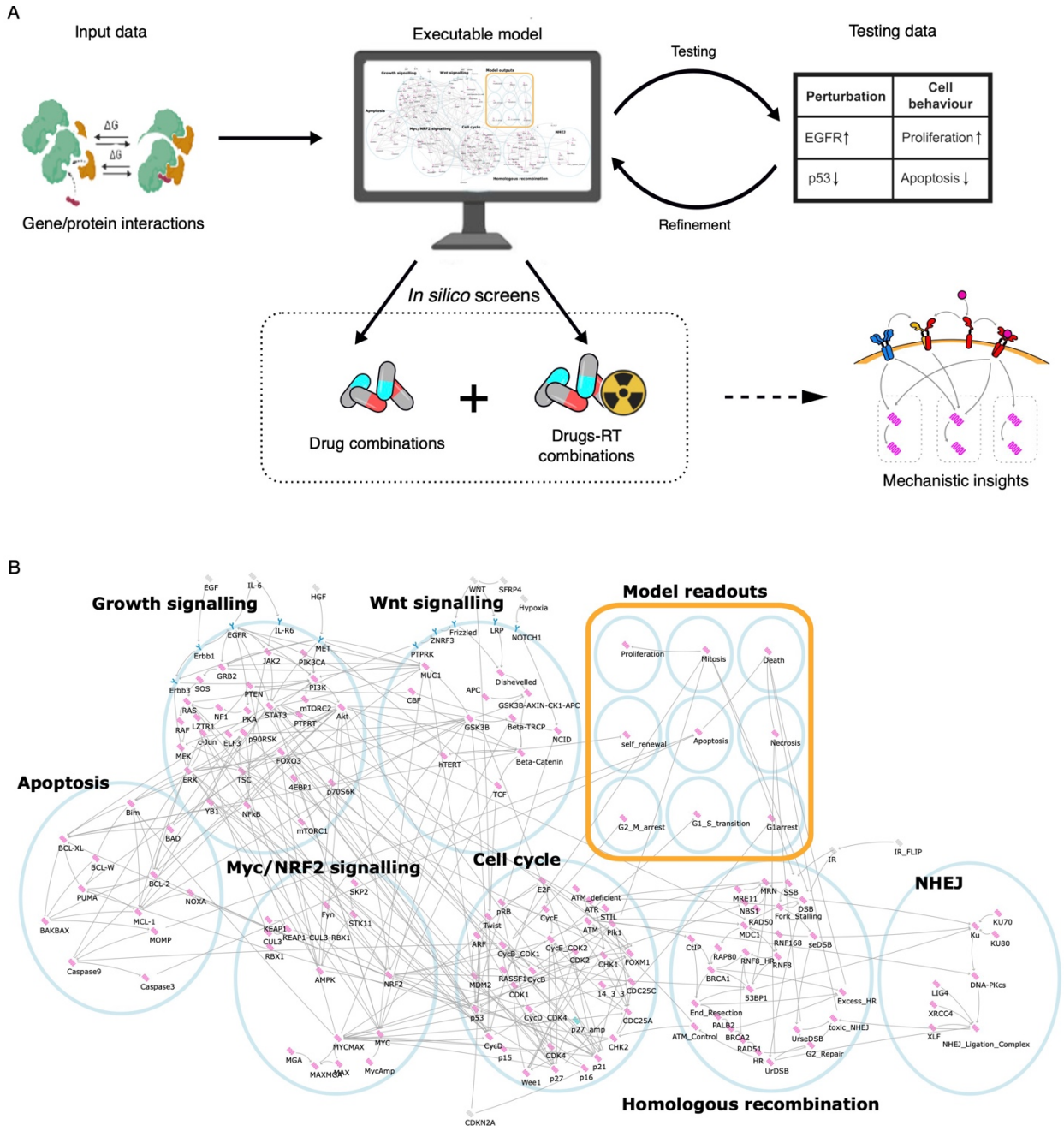

Figure 1. Outline of the workflow and executable NSCLC adenocarcinoma model. A) Schematic showing the workflow used to construct, test, and analyse the model. **B)** A network visualising the architecture of the executable model as seen in the BMA tool. Different subnetworks are enclosed by a blue circle, model inputs are coloured grey, receptors are coloured blue and cytosolic proteins are coloured pink. Edges represent regulatory interactions between proteins and are pointed for activating edges (→) and blunt for inhibiting (⊣). The phenotypic readouts are shown enclosed in a yellow box.

The NSCLC adenocarcinoma network model reproduces experimental data

To train the model, we collated a list of 26 publications reporting the behaviour of NSCLC adenocarcinoma cell lines under different experimental conditions, separate from and not used to build the model. These publications describe the behaviours (e.g., growth rates, levels of

apoptosis, protein levels) of different cell lines under perturbation by drugs and/or radiation. Cell lines were modelled by setting the nodes that represent genes with known driver mutations to the appropriate constant value (0 for loss-of-function and 3 for gain-of-function). Cell line mutation data were drawn from Cell Model Passports[25] and our own experiments (see Methods, Supplementary Table S4 and Supplementary Figure S1). We then used the model to find the stable states of the system, which we compared to the phenotypes measured in the experiments. Comparison of the simulated behaviours with the published observations was used to iteratively improve the target functions of the nodes within the model until the model recapitulates the behaviours observed in the published experiments (see Methods, Supplementary Table S5). We also modelled the sensitivity of six cell lines to single drug treatment with and without radiotherapy (HCC44, NCIH1373, NCIH23, NCIH358, NCIH1792, SW1573) and compared to the published literature, to test the DNA-damage repair section of the model (Supplementary Figure S2, S3). We examined common targeted therapies including EGFR[26,27], MEK, MET,[28] and DNA-PK inhibitors[29,30] and further verified that the model reproduced the effects of knock-out experiments on key proteins in oncogenic processes, including KRAS[31–34], MUC1[35], NRF2[36,37], JAK2[38], RAD51[39], ATM[40], RNF8[41], NOTCH1[42] and TP53[32]. When comparing the model behaviour to these published experiments, we see an accuracy of 91% (Supplementary Table S5, See Methods).

To identify treatments that maximise the difference, for the same dose, between the effect on cancer and healthy cells (maximise the therapeutic window) we also simulated healthy lung cells. We assume that the signalling processes in these cells are the same as in lung cancer except without driving oncogenic mutations. We tested this assumption by comparing to published experiments conducted using the immortalised epithelial lung cell lines HBEC3 and BEAS-2B[32,43] (Supplementary Table S4). Having reproduced existing experimental data, we next used the model to systematically predict the effect of unseen combinations of knock-outs in our panel of NSCLC adenocarcinoma cell lines.

Targeted monotherapies inhibiting Erbb1, RAS and STAT3 have an effective but narrow therapeutic window

To simulate personalised therapies with single targeted drugs, we systematically set the value of 95 druggable (see Methods, Supplementary Table S6 and Supplementary Figure S3) nodes in the model to 0 in six NSCLC adenocarcinoma cell lines (SW1573, NCIH1792, HCC827, PC9, A549 and NCIH1993) chosen for a range of driver mutations to reflect the genetic heterogeneity of NSCLC (See Supplementary Figure S1). By setting the value of nodes to a constant value of 0, we mimic the effect of inhibitors that could be used as targeted therapy. Overall, we observed that cancer cells are more resistant to targeted therapy than healthy cells when considering both cell proliferation and death levels (Supplementary Figure S2). Perturbations that are effective at killing cancer cell lines are those that directly target proteins downstream of activated oncogenes specific to those cell lines (e.g., EGFR in HCC827 and PC9 or KRAS in NCIH1993, NCIH1792 and A549), however, these treatments are also lethal to healthy cells. Inhibition of STAT3 kills cells in the A549 and NCIH1993 cell lines (Supplementary Figure S2C), a pattern observed with all other potential treatments demonstrating how small differences in mutational profile can lead to total resistance to therapy.

When identifying potential cytostatic treatments, we identify more potential drug targets. This includes inhibiting MYC, which limits oncogenic growth to the basal growth rate of healthy cells while
also reducing apoptotic signalling in all cell lines profiled apart from A549. In general, we see that healthy cell lines are more susceptible to treatment via the inhibition of single proteins than cancer cells (Supplementary Figure S2C). This underlines the importance of using combination therapies to maximise the perturbation space to find cancer-specific treatment options with a good therapeutic window.

NRF2 inhibition is predicted to protect healthy cells while 53BP1 inhibition sensitise cancer cells to radiotherapy

We next sought to assess combining targeted therapy with radiotherapy to see whether this would improve predicted treatment efficacy. We therefore used the model to assess the radio-sensitising effect of gene knockouts and compared the predictions to an *in vitro* CRISPR screen of radiation sensitive and resistant lung adenocarcinoma cell lines (HCC44, NCIH1373, NCIH23, NCIH358, NCIH1792, SW1573). We set one node at a time to a constant value of 0 to mimic a knock-out, in addition to cell line-specific mutations (Supplementary Table S4), and compared this effect with or without radiation, modelled through the value of the 'IR' node, (Supplementary Figure S3). The effect of IR is modelled through the induction of single-strand breaks (SSB), double-strand breaks, and replication-induced or single-ended double strand breaks (seDSB)[44]. We modelled the impact of SSB on fork stalling and collapse, and the subsequent generation of seDSB[45] as well as the downstream repair of DSB and seDSB by homologous recombination and non-homologous end-joining[46], with unrepaired breaks and toxic chromosome fusions leading to increased cell death. We define an effective radio-sensitising knockout as one that leads to more cell death as part of a combination compared to either the gene knockout or radiotherapy alone. We term the additive difference between cell death in the combination treatment and the most effective of these two monotherapies as ‘radio-sensitisation’ (see Figure 2A).
The model predicts broad classes of radio-sensitising knockouts. Some knockouts are radio-sensitising in both healthy and cancer cells; primarily inhibition of the NHEJ pathway, as expected[47]. Other known treatments such as ATM inhibition[48] are radio-sensitising across all cancer cell lines, but we also see cell line-specific radio-sensitising knockouts. For example, 53BP1 inhibition is particularly additive in SW1573 (Figure 2A-B). Such cell line specific behaviour demonstrates the difficulty in maintaining an effective therapeutic window across diverse patient mutations, and underlines the requirement for tailored therapeutic approaches to diverse mutational profiles.

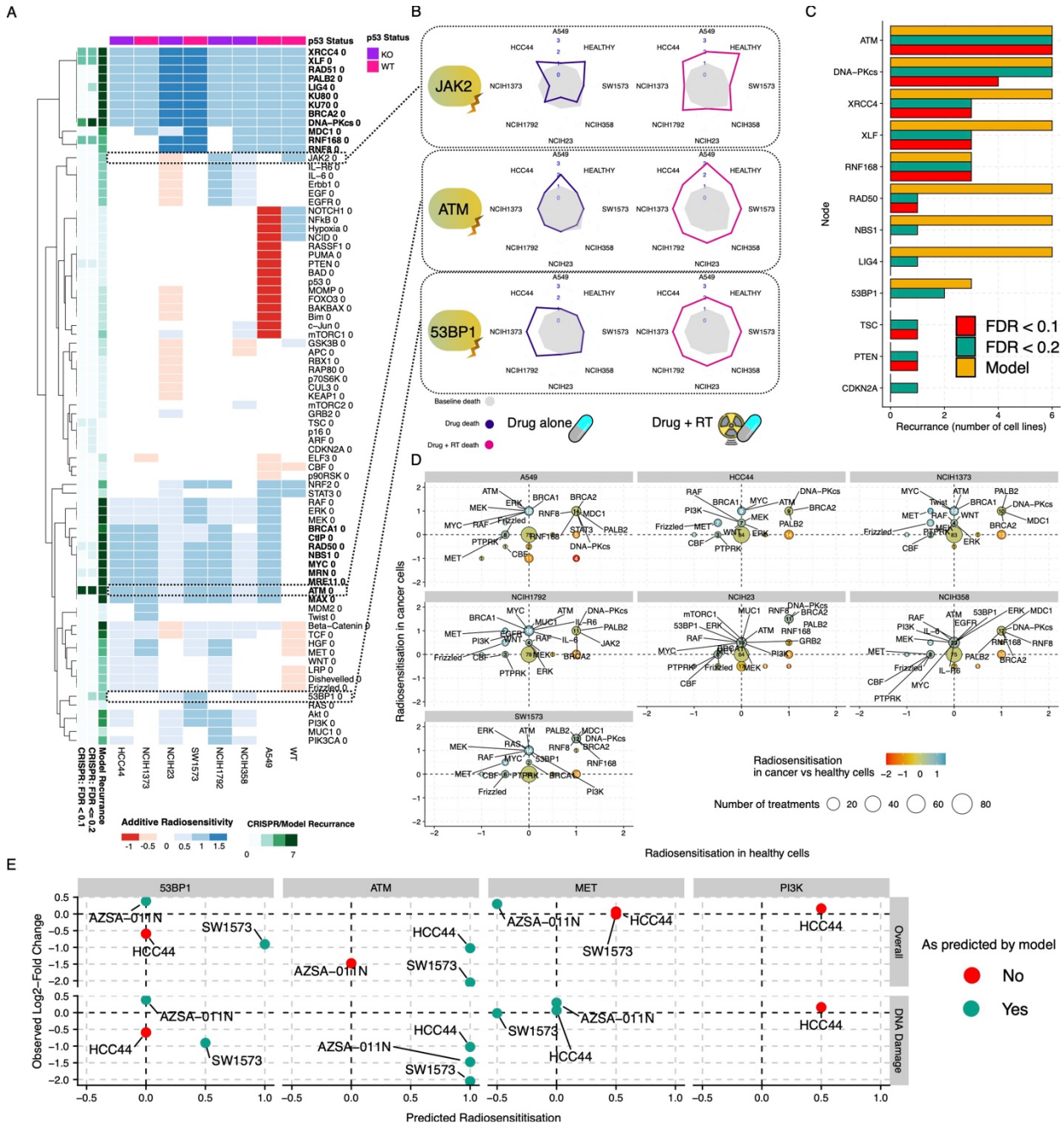

Figure 2. Systematic screen of perturbations on the *in silico* model reveals inhibition of ATM and 53BP1 as radio-sensitising agents. A) A heatmap showing predicted radio-sensitising effect *in silico* knockouts (rows, where the node value is set to 0), on NSCLC adenocarcinoma cell lines (columns). Radio-sensitisation is the increase (blue) or decrease (red) in cell death in the combination of IR and knock-out compared to the most effective of IR or knock-out applied alone. Side panels (green) show the number of cell line backgrounds in which the treatment was radio-sensitising in the model or the CRISPR screen (at FDR ≤ 0.2 and < 0.1) where we count a recurrence if radiosensitivity is observed at this threshold for any timepoint in the screen. Knockouts that confer broad radiosensitivity are shown in bold. **B)** Radar plots showing the levels of death after drug treatments (for ATM, 53BP1 and JAK2) (dark blue) and after drug treatment and irradiation (magenta) compared to the baseline (grey). Specific drug combinations that are broadly radio-sensitising across backgrounds are outlined in black in the heatmap in panel A. **C)** Number of cell lines in which knockouts were predicted to be effective in: the network model (yellow), CRISPR screen with FDR ≤ 0.2

(green), or CRISPR screen with FDR < 0.1 (red). Note: p16 and p14ARF knockouts were both observed to be effective in the CRISPR screen. These are both controlled by the CDKN2A node in the model and so are grouped under that node. **D)** X-axis change in healthy cell radio-sensitivity. Y-axis relative change in cancer cell radio-sensitivity. Blue is more radio-sensitisation of cancer than healthy; red is more radio-sensitisation of healthy than cancer. Point size is the number of knockouts that have this effect. **E)** Observed Log2-Fold-Change (y) vs predicted radio-sensitisation for genes in focussed CRISPR screen (x). Values shown are for maximum timepoint. Colour is blue for validation (FDR<0.1 for cases where model predicted sensitisation), red otherwise. AZSA-011N cells are healthy cell organoids. Any genes for which knockout was found to be essential at all timepoints were removed. Top row is predicted radio-sensitisation measured by change on overall cell death (measured by node 'Death'), bottom row is predicted radio-sensitisation measured by DNA-Damage specific cell death (measured by node 'Necrosis').

We compared the model results to an *in vitro* CRISPR screen in the six NSCLC adenocarcinoma lines treated with radiotherapy (HCC44, NCIH1373, NCIH23, NCIH358, NCIH1792, SW1573) (Figure 2C). The model correctly predicts those knockouts that led to radio-sensitisation in the *in vitro* CRISPR screen in 9 out of 12 cases (Figure 2C).

The model suggests that the radio-sensitising effects of knockouts outside of the NHEJ pathway are highly specific to mutational context, as we saw for many monotherapies (Figure 2A). In addition, when radiotherapy is applied, the model predicts similar levels of death in NSCLC adenocarcinoma and healthy cells (Supplementary Figure S3B-C). However, the degree to which a drug radio-sensitises a cell (the difference between the combination of IR and knock-out compared to the most effective of either IR or knock-out applied alone) is often higher in the cancer cells than the healthy cells. In particular, there is a subset of cases where all the death in healthy cells is driven by IR, but the majority of death in the cancer cells is driven by the combined effects of targeted therapy and IR. This suggests that by reducing the IR dose we could reduce the death in the healthy cells more than in the cancer cells and widen the therapeutic window. Combined with the personalised nature of radio-sensitisation, this prompted us to query the model for knockouts that lead to the largest change in radio-sensitivity.

Figure 2D shows the predicted additive radio-sensitisation of cancer cells versus healthy cells. Many treatments are predicted to radio-sensitise both cancer and healthy cells, for example those involved in DDR pathways. In the case of radio-sensitisation of cancer cells specifically, we predict that inhibition of MYC is particularly effective and specific. This is partly due to the essential role of MYC in proliferation[49], but also because of the regulation of NBS1 by MYC, which, as part of the MRN complex, plays a key role in coordinating the response to DNA damage.

Conversely, we predict that loss of members of the PTP family (e.g., PTPRT), leads to reduction in radio-sensitivity in healthy cells, protecting them from toxicity, while having no effect on many of the cancer cell lines. This is due to an increase in JAK/STAT signalling, with a concomitant increase in MCL-W that suppresses apoptosis, and NRF2, which aids in repair of radiation induced DNA damage. This has less effect in cancer cells as they have already up-regulated NRF2. We examined death from DNA damage (through the node 'Necrosis') specifically as this may play a greater role in response to different radiotherapy doses than apoptotic death (Supplementary Figure S3D). We predict that inhibition of NRF2 is particularly sensitising to DNA-damage associated death in cancer cells, due to reduction in DNA damage repair[50]. Equally, suppression of the KEAP1/CUL3/RBX1 complex leads to an increase in NRF2 in healthy cells, protecting them, without aiding cancer cells, as these over-express NRF2 via mutant KRAS.

To validate this, we test a selection of these genes, MYC, 53BP1, MET, PI3K and ATM in a focussed CRISPR screen in cancer cell lines (SW1573, A549, HCC44) and healthy cell organoids (AZSA-011N). Of these, MYC was unable to be tested as it proved essential in all cell lines. 53BP1 sensitised cancer cells and not healthy cells, in line with the model's predictions, although it sensitised both SW1573 and A549 relative to healthy cells, where we predicted it would be effective only in A549. ATM sensitised all cancer cell lines, as predicted, as well as healthy cells, which the model did not predict. MET did not show the expected sensitisation of the cancer cells (Figure 2E (top)), nor the protection of healthy cells (AZSA-011N). However, in our model we treat Apoptosis and DNA-damage associated death (Necrosis) separately. When examining the latter, we find that the model's predictions align well with observation in all genes and cell lines, other than for HCC44 in the case of 53BP1 and PI3K (Figure 2E (bottom)), although 53BP1 may be essential for HCC44 (essentiality was detected at early time points but not later timepoints).

ATM inhibition overcomes radio-resistance conferred by TP53 deficiency

As a key regulator of DNA damage response which is often mutated in cancer, we wanted to explore the association between TP53 mutational status and radiotherapy response in cancer cell lines. Accordingly, we simulated the cell lines from our radio-sensitisation screen with TP53 activated in cell lines where it has a loss-of-function mutation and inactivated in cell lines where it is competent (Supplementary Table S4). The model predicts that TP53 deficiency reduces death from radiation alone in most cell lines (Figure 3A, Supplementary Figure S4). However, when combined with a radio-sensitising knock-out, there are many potential combinations that are predicted to induce death in cancer cell lines regardless of TP53 activation, overcoming the radio-resistance due to TP53 loss-of-function (orange points on dotted line, Figure 3A).
ATM knock-out is an example of a radio-sensitising perturbation that is effective across all cancer cell lines, irrespective of TP53 mutation status (Figure 3B). Therefore, the model predicts that there is benefit in using radio-sensitising agents targeting those proteins identified in our i*n silico* knock-outs to improve the effect of radiotherapy for patients with a TP53 mutation. We experimentally validated these results by modifying SW1573 and NCIH1373 cell lines *in vitro* to flip the mutational status of TP53 (Figure 3C and Supplementary Figure S4A) Indeed, ATM sensitises cancer cells regardless of p53 status in all cancer cell lines for which this was tested in the focussed CRISPR screen (A549 and SW1573), as predicted.

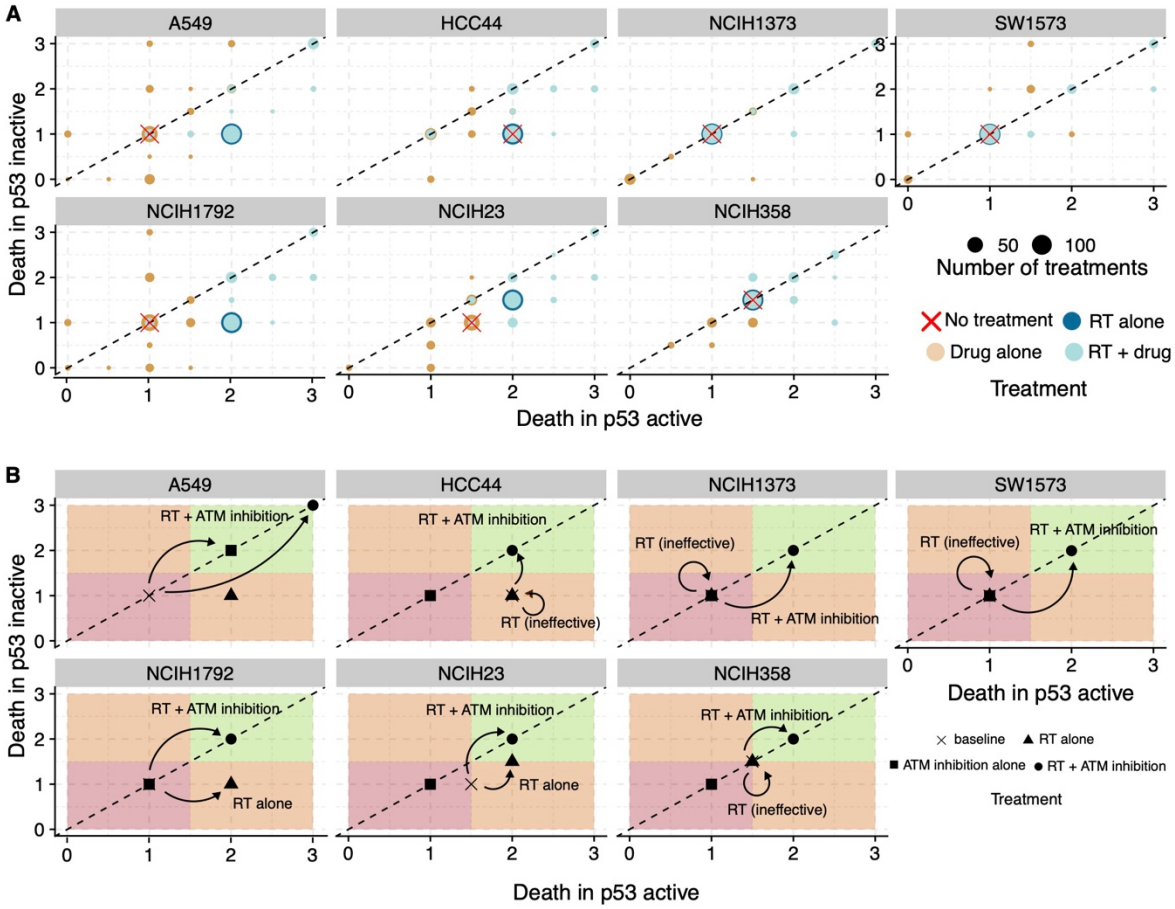

Figure 3. Radio-sensitising knock-outs increase death in a manner that is agnostic to TP53 status. A) Levels of death predicted by the models in cell lines that have been modified to have TP53 active (x-axis) and TP53 inactive (y-axis). Colours denote the type of treatment (dark blue for drug treatment alone, light blue for radiotherapy alone and orange for radiotherapy and drug treatment combined) and the size denotes the frequency of treatments in that position. Knock-outs below the dotted line are less effective in TP53 inactive cases then in TP53 active, knock-outs above the dotted line are more effective in TP53-inactive than active. **B)** Death in TP53 deficient (y-axis) and TP53 (x-axis) proficient cell lines showing the differences of radiotherapy alone and radiotherapy with ATM knock-out. Quadrants of the plots are coloured to denote desirable locations for therapeutic outcomes. Green indicates high cancer death regardless of TP53 mutational status, red indicates low death regardless of TP53 mutational status and orange indicates that knock-out efficacy is dependent on TP53 mutational status. Arrows show how in the case of ATM knock-out, the level of cell death with IR moves from below the dotted line i.e., less effective in the TP53 inactive case, to the dotted line, indicating that IR + ATM inhibition overcomes and neutralises the effect of TP53 inactivation.

350 **Predicted radio-sensitising targets stratify patient response to radiotherapy**

351 Following our systematic *in silico* screen of radio-sensitising knockouts, we observed that there
352 was a subset of genes that affect radiation sensitivity agnostic to mutational background. These
353 19 genes are marked in bold on Figure 2 and include members of the DNA damage repair
354 pathways (ATM, MDC1, XRCC6, XRCC4 etc) as well as transcriptional regulators (MYC and MAX).
355 We hypothesised that these candidate genes could be used to stratify patients as either
356 radioresistant or radiosensitive. To explore this, we used the TCGA database
357 (https://www.cancer.gov/tcga) of clinical data to see whether patients with low levels of gene
358 expression (as measured by RNA-seq) or copy number variation (CNV) for our predicted
359 radiosensitive genes survive longer after treatment with radiotherapy. We considered either of
360 these properties to be analogous to the activity of the node within our network model. Patients
361 with both low copy numbers (bottom 5%, n= 76) and of low RNA expression (bottom 10%, n=15)
362 for at least one radio-sensitising gene, compared to all patients, were determined to be
363 radiosensitive (Figure S5A, n=175).
364 When instead considering RNA expression and CNV separately, we found that with either
365 definition of activity of a gene we see a lower hazard ratio (longer survival) for patients predicted
366 to be radiosensitive after receiving radiotherapy (Supplementary Figure S5B-C, Cox proportional
367 hazards regression; HR= 0.4299, P=0.06 for expression and HR= 0.6421, P=0.08 for CNV). When
368 using both CNV and RNA to determine a consensus subset (see Methods) of radiosensitive
369 patients we also see a significant difference in survival (Figure 4A, HR= 0.5842, P=0.03),
370 suggesting that patients with a naturally lower activity of these genes have increased survival.
371 When looking at patients that have not received radiotherapy (n=705, Supplementary Figure
372 S5D) we see no significance (Supplementary Figure S5E-G), indicating that these genes are
373 stratifying patients only in the presence of radiation (Figure 4B), consistent with our model's
374 prediction of these targets as potential radio-sensitising agents.
375 Lastly, we investigated whether there was a continuous relationship between the lowest level of
376 a radio-sensitising gene in a patient and their survival following treatment with radiotherapy. This
377 assumes that the level of radio-sensitisation in a patient is rate-limited by each of our model-
378 predicted radio-sensitising agents. For each patient, we calculated the lowest linear copy number
379 of each of the 19 genes (Figure 4C) and then used this continuous variable to predict survival in
380 patients exposed to radiotherapy. The survival area plot for this analysis is shown in Figure 4D,
381 showing significant association between the minimum CNV level of the radio-sensitising genes
382 and survival (Cox proportional hazards regression; HR=2.91, P=0.07). This association does not
383 exist for survival among patients not treated with radiotherapy (HR=1.19, P=0.6), indicating this
384 relationship only exists in the presence of radiation. Collectively, these findings demonstrate that
385 low CNA and low RNA expression of our predicted radio-sensitising genes are significant
386 predictors of improved survival in patients receiving radiotherapy. However, our modelling and
387 statistical analysis of clinical outcomes also shows that many patients are radioresistant and so
388 this necessitates broader choices of therapeutic options.
389

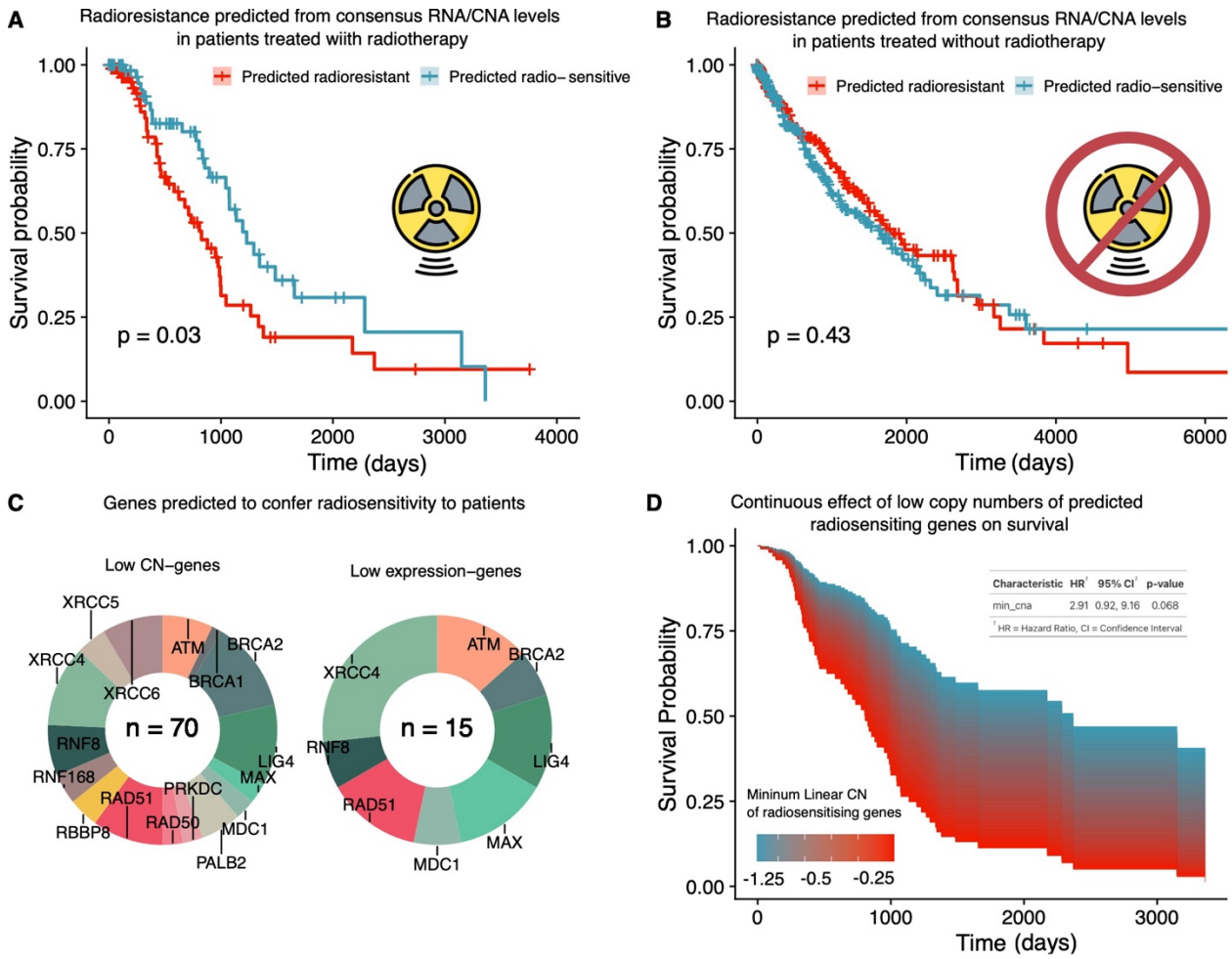

Figure 4. *In silico* predictions stratify radiation-treated patients into radiosensitive and radioresistant strata. A, B) Kaplan-Meier survival curves showing the differences in survival between predicted radioresistant patients (red) and radiosensitive patients (blue) for patients treated with radiation (B) and without radiation (C). The x-axis indicates the time (days) since diagnosis and y-axis indicates the survival probability. **C)** Pie-charts showing the genes with the lowest copy number (left) or expression (right) for each patient predicted to be radiosensitive. **D)** Continuously coloured survival area plots showing the effect of the minimum copy number of radio-sensitising genes on survival. The x-axis indicates the time (days) since diagnosis and y-axis indicates the survival probability. Colour indicates the minimum copy number of genes within our predicted set, with blue indicating lower copy number.

In silico screens identify MYC and ATR inhibitor as a cancer-specific treatment combination

To find further treatment combinations that are effective specifically on cancer cells we looked at different combinations of targeted therapies that could increase the difference in death between healthy and cancer cells. Combination treatments are also likely to reduce resistance compared to monotherapy[51,52]. We performed *in silico* screens of pairwise combinations of 95 druggable targets in the model for SW1573, NCIH1792, HCC827, PC9, A549 and NCIH1993 cell lines (see Methods). We isolated the treatment combinations that were predicted to have an additive effect on overall survival (proliferation - death) when compared to the most effective single treatment (see Methods and Supplementary Figure S6). This was measured for survival rather than death because combination therapy seeks to limit oncogenic growth as well as induce

411 apoptosis, as opposed to radiotherapy which has the primary aim of causing apoptosis or DNA-
412 damage associated death[53]. We then clustered these treatments into those that have a similar
413 effect on the cell lines to highlight patterns of response and profiles of sensitivity. This produced
414 24 different subclusters, labelled *I* - *XXIV*, in order of their efficacy vs the most effective single
415 treatment (see Methods). We see that clusters *I, II* and *IV* are the only broad-spectrum
416 treatments that have a wide, additive effect across all cell lines tested (Figure 5).
417 We next compared our simulated results to experimental data generated by Nair and colleagues
418 measuring the additive score of various drug combinations in SW1573, NCIH1792, HCC827, PC9,
419 A549 and NCIH1993 (Supplementary Figure S7)[54]. We see that the data shows significant
420 concordance with our predictions across all cell lines tested. Comparing Higher than Single Agent
421 effect (HSA) to our predictions of additivity, we see moderate, but significant correlation (Kendall
422 Tau = 0.16; p-value = 8.176e-11) across all drug combination predictions. Given the large
423 proportion of intermediate or no additivity predicted by our model and measured by Nair and
424 colleagues, we also looked at correlation of purely additive combinations as predicted by our
425 model (those shown in Figure 2). In these groups we see stronger correlation (Kendall Tau = 0.27;
426 p-value = 1.7e-07,). Correlations of the most additive treatments in Clusters *I* - *V* show stronger
427 correlation still (Kendall Tau = 0.37; p-value = 2.3e-07). For reference, the average Pearson's
428 correlation across experimental replicates in GDSC[55], CTD[56] and PRISM[57] drug screening
429 platforms is ~0.30[58]. We also find that the model's predictions can recapitulate the sensitivities
430 of different cell lines to specific drugs (See Supplementary Figure S8 and Supplementary Notes).
431 These results indicate that our predictions correlate with published data and correlation
432 improves when discriminating between more additive therapies.
433 According to the simulations, the most effective group of drug combinations by average additivity
434 across cell lines are those targeting AKT and MAPK pathways (Cluster I). These have a uniform
435 effect across cancer cell lines, increasing death from the untreated (baseline) level while also
436 causing growth arrest (Figure 5). This combination does not discriminate between oncogenic or
437 healthy cells, so although it is a reliable means of treating a wide range of mutational profiles in
438 cancer, it is also likely cytotoxic to healthy tissue. Cluster II discriminates between healthy cells
439 and tumorigenic cells and is composed of ATR and MYC inhibition. It limits growth to be on par
440 (proliferation = 1) with healthy cells, while increasing death only in cancer cell lines. The
441 remaining highly additive clusters are those dealing with RTKs mutated in specific cancer cell
442 lines. For example, Cluster *III* is additive in cell lines with *EGFR* gain-of-function mutations, while
443 Cluster *V* is additive in NCIH1993, a cell line with a *MET* mutation. These clusters illustrate the
444 importance of cell line-specific key genetic determinants of response that govern the most
445 effective and additive combinations needed for efficacious treatment. However, given drugs
446 within Cluster II are broadly effective regardless of mutational profile, while sparing healthy cells,
447 we decided to explore further the mechanism of action of this line of therapy.
448

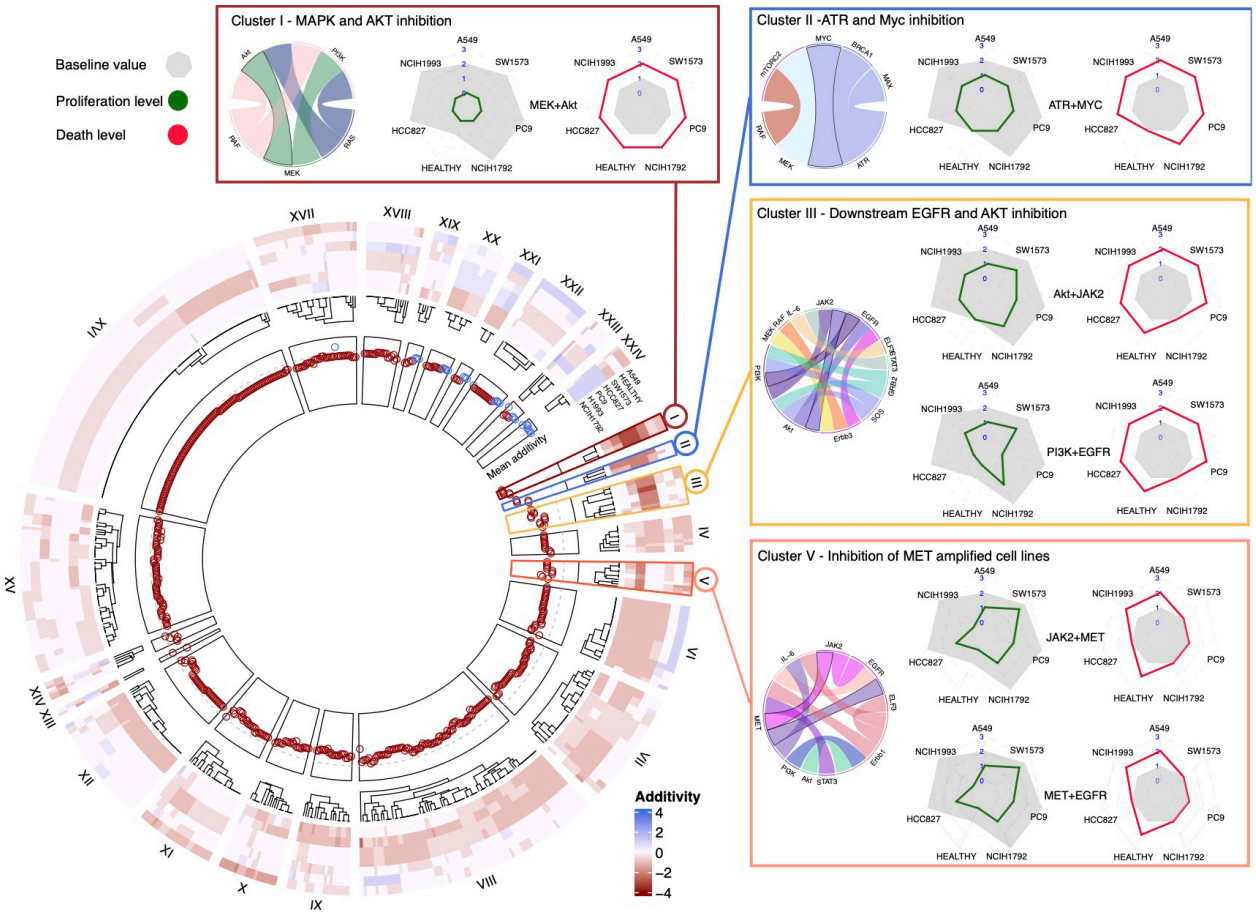

Figure 5. Systematic *in silico* combination screen on NSCLC adenocarcinoma network model. Circular heat map showing the additive effect of drug combinations on selected NSCLC adenocarcinoma cell lines. Columns (spokes of the wheel) are the drug combinations and have been clustered into groups (I-XXIV) of drugs that have a similar additive effect. Red indicates those combinations that have a greater additive effect, while blue represents those drugs with antagonistic effects (the drugs cancel one another out). The plot in the inner wheel of the circle shows the mean additive effect of a drug across all cell lines and is red for those drug combinations with overall additive effect and blue for those antagonising one another. Clusters I, II, III and V, and the most effective combinations within, them are highlighted. Circular chord diagrams illustrate the various drug combinations within a cluster and radar plots show the absolute levels of proliferation (green) and death (red) after drug treatment when compared to the baseline (grey). These are shown for specific drug combinations that are outlined in black in the chord diagrams.

Combined MYC and ATR inhibition is predicted to limit cell growth and kill cancer cells through double stranded breaks

The model predicts that inhibiting MYC limits proliferation and causes cell death when combined with ATR inhibition in cancer cell lines without affecting healthy cells. This is in line with our earlier prediction of the effect of MYC inhibition in combination with radiotherapy. ATR inhibition alone is predicted to have little impact on all cell lines tested, whereas MYC and ATR inhibitions are predicted to increases cell death in cancer cell lines more than in healthy cells (Figure 6A). To assess the effect of these perturbations on the entire model state, we used Principal Component Analysis (PCA) to visualise the entire state space of the model following treatment with ATR and MYC inhibitors (Figure 6B), seeing that the treatment predicts to affect healthy cells (bottom left)

471 less, while leading to a large difference in cancer cell lines (top). The loadings for different model
472 variables are also plotted as vectors to highlight those that contribute to the separation in
473 coordinate space of the PCA and represent variables that are changing mostly after perturbation.
474 We predict that following treatment there is an increase in p15, G2/M arrest and toxic NHEJ,
475 which is responsible for the increase in cell death. The variables and the regulatory interactions
476 that exist between them are plotted in Figure 6C. This suggests how ATR and MYC inhibitions
477 combine to limit oncogenic signalling, as well as the induction of DNA damage-associated death
478 in cell line PC9 (the remaining cell lines in Supplementary Figure S9). MYC inhibition is predicted
479 to disrupt the oncogenic operation of the cell cycle, while also inhibiting apoptosis and
480 homologous recombination. Inhibiting ATR could then increase single-ended double strand
481 breaks (seDSB) by preventing the cell from responding properly to replication stress, which is
482 higher in cancer cells due to their higher rate of proliferation. MYC inhibition prevents proper
483 repair of seDSB owing to the loss of MRN and thus ATM activation, leading to toxic NHEJ[46].
484 Healthy cells are also predicted to be less affected by the inhibition of MYC, which is more highly
485 activated in every cancer cell line (Figure 5C). As a result, inhibition of MYC and ATR is predicted
486 to have the greatest therapeutic window of all the treatments we simulate and could be a
487 promising therapeutic candidate applicable to a wider variety of mutational backgrounds.
488 As of writing, MYC inhibitors are in early stage trials[59–61], however, other specific drug
489 combinations that we predict to be additive are composed of clinically approved drugs. Unlike
490 MYC and ATR inhibition, these treatments are only effective in selective cell lines. To explore this
491 effect more systematically, we investigated the key explanatory mutations in cell lines that drive
492 responses to various groups of targeted therapy combinations that we predicted as being
493 additive.
494

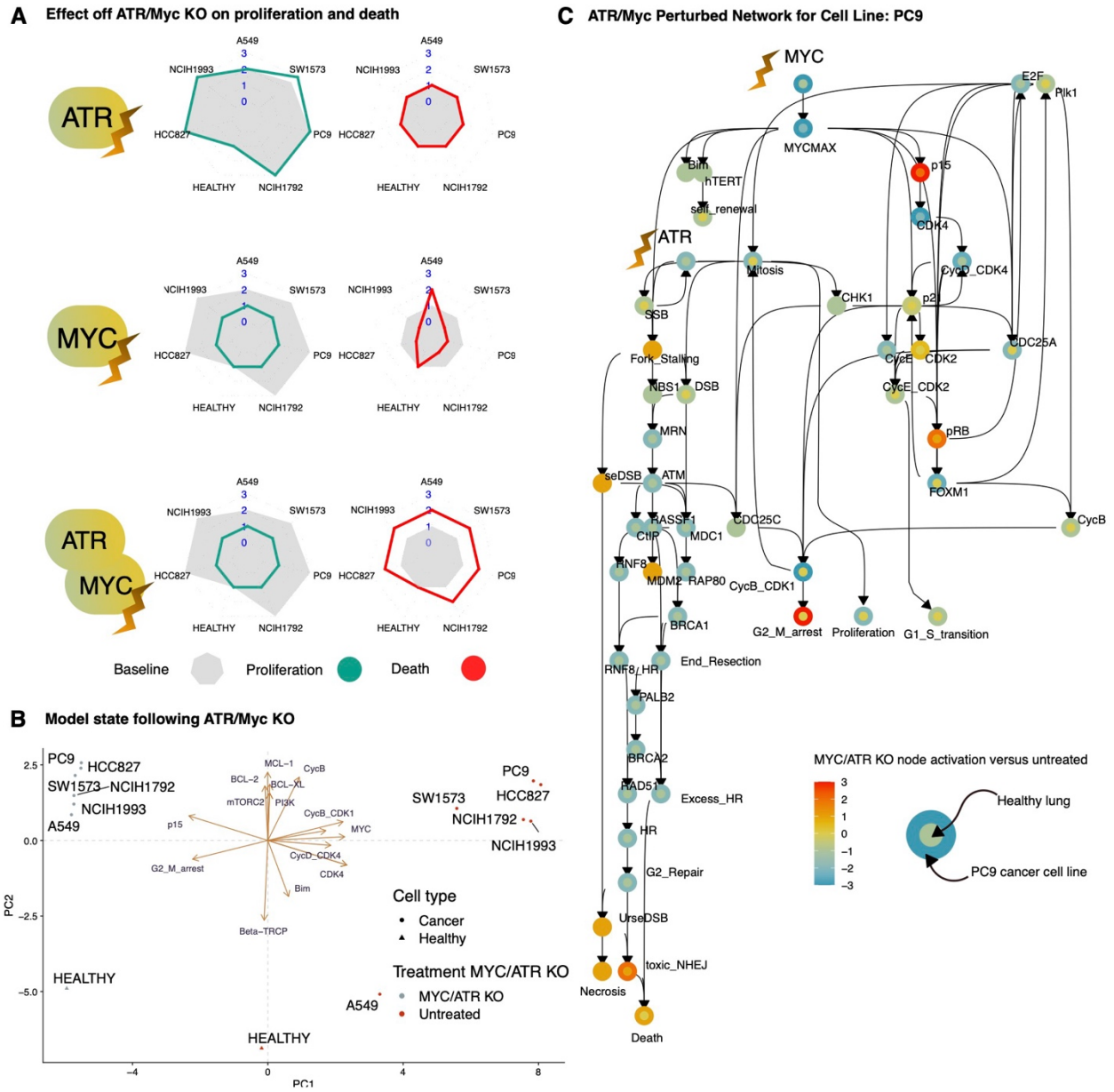

Figure 6. Mechanistic analysis of combined ATR and MYC inhibition illustrates their induction of DNA damage associated death. A) Radar plots showing the absolute levels of proliferation (green) and apoptosis (red) after MYC inhibition, ATR inhibition and combined MYC and ATR inhibition. The baseline growth and proliferation are shown in grey. **B)** PCA showing the model states of different cell lines following treatment with MYC/ATR inhibition. Cancer cell lines are plotted as circles and healthy cells (lacking oncogenic mutations) are triangles. Untreated cells are in red and treated cells are in red. Vectors are also included in the PCA to visualise the loadings of different variables and how they contribute to the separation of *in silico* samples in 2D space. **C)** Subnetwork of the model, covering the proteins and variables that changed after treatment of MYC/ATR inhibitors in PC9 (a cancer cell line). Colour of the node illustrates the difference between ATR/MYC inhibition vs untreated (blue for a relative decrease in activation and red for an increase) in PC9 (outer circle) and the difference in healthy lung cells (inner circle).

EGFR and TP53 mutations explain additive response to combined MAPK and AKT inhibition

Given that treatment effectiveness varied with small changes in mutational profile, we aimed to find which mutations have the greatest explanatory power in drug response, as these could be used as biomarkers. Accordingly, we visualised drug additivity in the most effective combination clusters and aligned this with the mutations used to model the cell lines (Figure 7A). We predict that EGFR is strongly associated with response to treatments in clusters *I, III* and *V*. For example, treatments in cluster *I* (MAPK/Akt inhibition) are most additive in PC9 and HCC827 (EGFR mutant cell lines). Similarly, treatments in Cluster *III* are most additive in cell lines that contain EGFR gain-of-function, while the opposite is true for Cluster *V.* Additionally, TP53 mutations are associated with response to clusters I, and III with the most additive responders to those clusters of combinations being NCIH1993, HCC827 and PC9 (Figure 7A).

We used a linear model to quantify the relationship between cell line mutations and their responses to combination treatments and find the most explanatory mutations for additive drug combinations responses in the different cell lines (See Methods). We found that TP53 and EGFR mutations are most broadly associated with an additive response to the tested combinations (Figure 3B). However, for Cluster V we see a negative coefficient for EGFR mutations, indicating that the absence of this mutation is required for additivity to be observed. Instead, a MET amplification (as is the case for NCIH1993) is associated with additivity in this cluster (Figure 7B). These results suggest which mutations determine response in different mutational profiles, and highlight EGFR, TP53 and MET as key for patient stratification. Such insight is key to bridging therapeutic responses and oncogenic mutations, allowing us to stratify patients to find the most suitable course of treatment for a given situation.

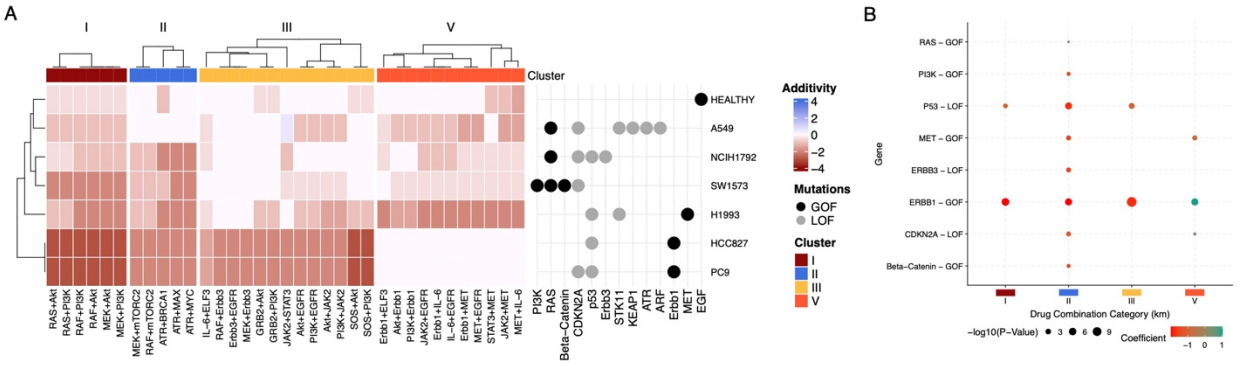

Figure 7. EGFR and TP53 mutations explain the response of cell lines to targeted combination therapy. A) Heatmap illustrating aligning the mutations of cell lines (right) with their response to the most effective drug combination clusters from Figure 5 (I in red, II in blue, III in yellow and V in orange). Columns of the heatmap indicate specific drug treatments and rows indicate cell lines. The colour in the heatmap refers to additivity with red indicating strongly additive behaviour and white indicating no additivity. The schematic (right) shows mutations as columns and cell lines as rows, with gain-of-function mutations for a cell line and loss-of-function (grey). **B)** Plot showing the coefficients of the linear model relating mutations present in a cell line (y-axis) to additive response against drug clusters (x-axis). Colour represents the value of the coefficient, such that blue indicates a mutation is associated with additive response to a cluster and red indicates that a mutation's absence is associated with additive response to a cluster. Size of the dot represents the significance of the association.

Discussion

Matching the variety of mutational profiles exhibited by NSCLC adenocarcinoma with the wide range of existing and potential therapeutic options presents a huge combinatorial challenge. Here, we showcase an *in silico* platform for executable modelling to explore this immense therapeutic landscape. By using the broad and extensive prior knowledge from published experimental research, we constructed an executable model that can explore treatment options in an efficient and mechanistically interpretable fashion. Using this platform, we assessed ~66,000 predicted combinations of targeted therapy and radiotherapy, finding the most suitable and effective treatment options, specific to given genotypes. We also investigated how mutations combine and determine response to therapy, and the mechanisms that underpin this, allowing for testable hypotheses to expand our understanding of oncogenic signalling, and demonstrate a novel method for stratification of patient sensitivity to radiotherapy using clinical data based on targets identified by the *in silico* model.

Finding that healthy cells are more sensitive to single-agent treatment than cancer cells in our *in silico* modelling and motivated by the need for combination treatments to prevent resistance[51] we explored combinations of drugs with one another and with radiotherapy. We find that the most effective cluster of drug combinations (Cluster *I*) consists of combined MAPK/PI3K inhibition. AKT and MAPK are downstream processors of all growth pathways in the *in silico* model and most oncogene mutations found in lung cancer target members of these pathways or upstream regulators (e.g., KRAS, PIK3CA, EGFR, MET, ALK). MAPK/AKT inhibitors are often used as positive controls for synergy experiments and have previously been flagged as highly additive in lung cancer[54,62]. However, healthy cells also rely on these pathways and so their inhibition can cause side-effects[63]. We were able to identify other combinations that specifically targeted cancer cells owing to mutations in the NSCLC adenocarcinoma cell lines. Specifically, we found that EGFR is an important determinant for the additive response to several potential combinations. We also find that absence of EGFR mutation is as an important determinant of response to MET inhibitor combinations than the presence of a MET mutation itself. In general, we show that the mutational status of receptors is important in determining additivity to targeted therapy, and so a patient's mutational status of EGFR, MET among others are particularly informative in determining personalised therapeutic options.

Most combinations have a similar effect on healthy and cancer cells. However, for both radiotherapy and combinations of targeted therapy, we predict that MYC has strong potential in targeting cancer cells without affecting healthy cells. MYC is frequently overexpressed in cancer, owing to its central position in the hourglass topology of pathways governing regulation and effect[64]. This importance makes resistance to MYC-targeting drugs extremely difficult[65]. This structure is reflected in our model and means that for the heterogeneity of cancer mutational profiles, they broadly produce a higher activation of MYC and its downstream targets[65]. This puts MYC in a unique place as a promising therapeutic target with inhibition well tolerated in healthy tissue[66]. However, despite advances in developing inhibitors targeting MYC[67,68], none are currently clinically approved for treatment. Our work underlines the exciting prospect of MYC as a therapeutic target and goes further in suggesting ATR as a parallel target, offering the option to further exploit weaknesses in cancer cells DNA damage repair. We show that by targeting cancer cell reliance on MYC overexpression and the dependence of DSB

586 repair on MYC via the MRN complex, one can produce therapeutics that are robust and broadly
587 effective against varied mutational profiles. However, this depends on how sensitive DDR
588 pathways are to MYC inhibition as MYC inhibitors such as Peptomyc[61] and OMO-103[69] are likely
589 to be less effective compared to the full knockout simulated by the *in silico* model. Our model
590 suggests that the effect of MYC inhibition on cancer cells is due, in part, to its regulation of DSB
591 repair via the MRN complex. Prior work in cell lines found that DDR was robust to MYC
592 downregulation[70]. Our analysis shows that a clinical signature (derived from *in silico* simulations)
593 including MYC and its binding partner MAX act as a predictor of radiosensitivity (Figure 4A).
594 Together these results suggest that the link between MYC and radio-resistance should be
595 investigated further.
596 Radiotherapy remains a main component of the standard of care for NSCLC adenocarcinoma
597 treatment[1]. A key factor in response to radiotherapy is TP53, with mutations disabling its
598 activation, either in the TP53 gene or upstream, frequently seen across all tissues and often
599 associated with therapy resistance[71,72]. The exact effect on radio-sensitisation is contentious,
600 with TP53 loss-of-function often leading to radio-resistance[73,74], but contributing both to radio-
601 sensitivity and radio-resistance in different contexts and tissues[75–77]. We predict that TP53 loss-
602 of-function mutations in NSCLC adenocarcinoma are broadly radio-protective, yet in the
603 presence of specific mutational profiles can be radio-sensitising. A subset of potential treatments
604 is radio-sensitising despite TP53 mutation, and some are completely invariant to it (Figure 3B).
605 This suggests that radio-resistance can be overcome, or pre-empted, by identifying the correct
606 treatment and offers hope that this may hold with a broader range of resistance mechanisms.
607 Due to the increased toxicity of radio-sensitising treatments, we predict it will be important to
608 stratify patients by TP53 mutation[78] for drug-radiotherapy treatments. TP53 mutation occurs
609 early in NSCLC adenocarcinoma[79] and is strongly associated with metastatic seeding sub-clones.
610 As metastases are the key driver of patient death[80], treatments that target clones that are
611 mutated in drivers of metastases are especially important. Our identification of radio-sensitising
612 treatments that overcome TP53-driven radio-resistance satisfies a key part of this. We further
613 use our model to identify a 19-gene signature that, by combining CNV and RNA-expression data,
614 stratifies patients into radiosensitive and radioresistant groups. We suggest this can be used to
615 better target radiotherapy treatment to those patients that are most likely to benefit from it in
616 the clinic.
617 Radio-sensitising combination treatments are already being explored on a small scale, for
618 example as part of the CONCORDE clinical trial[81], and we demonstrate the potential of this
619 approach with our large scale *in silico* and *in vitro* screens. We validate our *in silico* model
620 predictions in a focussed CRISPR screen and find that the model prediction of DNA-damage
621 related cell death is a good indicator of sensitisation. We were unable to test our predictions in
622 cases where gene knock-out was lethal to cells without radiation, e.g., in the case of MYC. Such
623 knock-outs are less well tolerated than intervention with drugs, as demonstrated by MYC
624 inhibitors such as Peptomyc[61] and OMO-103[69] being well tolerated in clinical trials, and so further
625 studies with inhibitors may prove fruitful. Calibrating contributions for targeted treatments and
626 IR on different mechanisms of cell death (i.e., apoptosis vs DNA-damage associated cell death) is
627 challenging. Indeed, we find that our model is more accurate when we output DNA-damage
628 associated cell death and apoptosis separately. It is of especial note that inhibition of 53BP1 leads
629 to radio-sensitisation in cancer cell lines but not in healthy cells. 53BP1 loss is a common

resistance mutation to PARP inhibitors[16], and thus this may suggest a collateral sensitivity that can be exploited for second line treatments.

Current experimental approaches to identify combinations of therapies involve performing global screens of perturbations on various cell models of NSCLC adenocarcinoma with differing mutational profiles. This can be done with drugs or CRISPR knockouts alongside 'omics measurements, observing the survival of the treated cells to understand hidden mixtures of lethal targets[54,62,82]. For example, Jaaks *et al.* tested 2025 pairwise drug combinations *in vitro* using the Genomics of Drug Sensitivity in Cancer (GDSC) cell line screening platform to identify biomarkers of response to combination therapies[55,83]. While such screening strategies can yield extremely high throughput, identifying target hits and biomarkers of their response across a broad range of unrelated backgrounds, there are practical drawbacks of such approaches. For example, developing a mechanistic understanding is hampered by off-target effects in drugs and CRISPR guide RNAs[84], which can lead to false positive[85] and false negative results[86]. Additionally, these screens are time-consuming and expensive and cannot be performed on rarer genetic profiles easily, leading to results biased towards the most common cellular models.

Computational methods can circumvent some of these technical issues and provide complementary screening approaches. For example, Eduati *et al.* use perturbation screening data to train a network to uncover patient-specific mechanisms underpinning pancreatic cancer[87]. Their model was trained using perturbation screens of patient biopsies and tested pairwise combinations of 12 targetable nodes in the network. In our work, we build on this by using more coarse-grained, but large-scale modelling of biological processes, allowing for more targetable nodes (i.e., 95 druggable targets), and integrated radiotherapy. Our modelling approach also only require mutational data for individualisation of our generic model, rather than training on combinatorial perturbation screening on cancer biopsies, which are more expensive and invasive and have limited clinical applicability. Fröhlich *et al.* used a larger, pan-cancer mathematical model to predict effective drug combinations[88]. However, the complexity of the parameter space of these models makes them computationally intensive to run on novel mutational backgrounds and mathematical models with many parameters more prone to overfitting than coarse-grained executable biological models. Others have used phospho-proteomic changes[62] and machine learning[89] to predict drug sensitivity. However, while the accuracy of the method was high[62], it is not clinically feasible currently to take phosphoprotein measurements of patients to determine drug response. Moreover, machine learning based approaches used to predict synthetic lethal targets lack the mechanistic interpretability of this method and often neglect radio-therapeutic combinations due to the relative lack of genome-wide data on radiotherapy sensitising agents. Our *in silico* model incorporates radio-resistance which is important to consider as it is already a common clinically used therapy.

In this study we demonstrate how executable modelling enables system-level experiments to be rapidly conducted. In addition, our *in silico* approach allows mechanistic transparency, providing insight into why treatments do and do not work and the biological underpinnings of mutational profile-specific sensitivities. Using mutational data, our executable models can be individualised, paving the way for 'digital twins' of tumours for testing hundreds of thousands of therapeutic options. We envisage that executable models have the potential to improve personalised therapy in NSCLC adenocarcinoma patients and help predict and combat the development of resistance to treatment.

Methods

We performed all visualisation and data analysis using the programming language R, and data visualisation packages ggplot2, ComplexHeatmaps and Circularize. Figure 1A was created with BioRender.com.

Qualitative networks

We represent the NSCLC adenocarcinoma signalling network as a discrete qualitative network[22]. This represents each gene, protein, or process as a node with multiple finite values of the range (0-3), where 0 represents very low activity e.g., due to a loss-of-function mutation, 1 represents normal behaviour, 2 elevated activity and 3 represents very high activity e.g., due to a gain-of-function mutation. This was built, tested, and analysed using the open source webtool, BioModelAnalyzer (BMA, https://biomodelanalyzer.org) and associated command line tools (https://github.com/hallba/BioModelAnalyzer).

Nodes in the network represent biological factors such as proteins or subunits of proteins. Input nodes represent growth factors, or in some cases amplification as with ATM. Output nodes are representing phenotypes such as death and proliferation. Regulatory interactions (both activating (→) and inhibitory (⊣)) are represented by edges between nodes. The level of activity of a node responds to the upstream levels of regulators of that node. This is determined by a mathematical function, unique to each node that integrates the levels of the upstream regulators to determine the target level of the target node at the next time-step, with the activity of each node changing by at most 1 unit per time step. This function is termed the target function. The default target function is the average of the activating upstream regulators, negated by the average of the inhibiting regulators (*avg(pos)-avg(neg)*). More complex functions are used as needed to recapitulate specific experimental behaviours (see below). These target functions along with corresponding references are described in Supplementary Table S2. A summary of the nodes included, and their HUGO gene symbol are summarised in Supplementary Table S3.

For a specified starting state of all nodes, the model will update node values synchronously, such that there will be one deterministic stable attractor of the network. This attractor can be a fixed-point attractor with one end state, or it can be a loop of states that the model cycles through, called a cyclic attractor. We test the model from all possible initial states, which allows for multiple attractors to be reachable, termed a bifurcation. In the case of a loop or bifurcation, the upper and lower bounds across all attractors are returned. This is done using the algorithm described in Cook *et al.*[90]. The algorithm for network simulation is found in Schaub *et al.*[22]. If there is no single attractor, we use the midpoint of the upper and lower bound as an approximation of the overall level of the node.

Model construction and testing

Experimental evidence for each model edge is described in Supplementary Table S1. We manually curated a separate set of 26 papers describing the behaviour of different NSCLC adenocarcinoma cell lines under various perturbations and conditions. From these papers 69 separate experimental conditions were modelled and used to optimise the target functions of the model. This is described in Supplementary Table S2. Accuracy was calculated by taking the number of experiments recapitulated, versus the total number of experiments. An experiment was

715 considered recapitulated if the predicted direction of change of the model is the same as that of
716 the experiment.

717 **Mutational profiles for all cell lines were drawn from Cell Model Passports**

718 To model cell lines we used mutational data from Van der Meer *et al.* as of 04/01/2023[25].
719 Mutations were modelled if they were listed as a driver or a deletion for a node in the model. If
720 annotated as a gain of function the respective node was set to the maximum value, if a loss of
721 function or a deletion the node was set to zero, except in the case of ATM. After the results of
722 the first CRISPR screen, we observed that ATM knock-out was still effective in NCIH1373 and
723 NCIH23 cells despite an ATM mutation observed in both, therefore we model this as a deficiency
724 but not complete homozygous knockout of ATM. We focussed on annotated driver genes and
725 complete deletions so as not to over-specify the model, and to focus on those changes that were
726 likely to be consistent within the population of cell lines[91].

727 **Mutational profiling of cell lines used in radiotherapy CRISPR screens**

728 Mutational data was derived using publicly available datasets, principally DepMap and
729 corroborated using western blotting (*e.g.*, TP53 status). Radiation sensitivity was assessed using
730 colony forming assay, and longer-term cell viability assays (e.g. cell-titre glo >7day timepoint) and
731 assessed against published literature.

732 **Modelling of combination and monotherapy**

733 To find effective treatments, we inactivate (set target function to a minimum) or activate (set
734 target function to maximum) all nodes representing druggable nodes in the network either singly
735 or in a pair-wise combination, using the BMA Command Line tool BioCheckConsole. For each
736 node in the network, we curated a list of drugs that could target nodes within the network,
737 finding 95 candidate drugs using the druggable proteome in The Human Protein Atlas
738 (https://www.proteinatlas.org/humanproteome/tissue/druggable; Accessed 04/08/2023). We
739 evaluate these perturbations by identifying the stable state of the network for death and
740 proliferation as outlined in the 'Qualitative Networks' section above. To have a single value to
741 predict cell growth we take the difference between Proliferation and Death.
742 For combination therapy we simulated these drugs together and studied their interaction using
743 a value we describe as additivity. This is analogous to the experimentally determined Higher than
744 Single Agent effect (HSA) and describes the growth of cells after combined drug treatment
745 relative to the most effective (minimum viability) of the individual drugs in the combination.
746 Combination treatments were clustered using the k-means algorithm to find groups of therapies
747 with similar levels of additivity across cell lines.

748 **Modelling of radiotherapy**

749 To model the effects of radiotherapy, we increase the `Radiotherapy` node to maximum. This
750 leads to increases in the single and double strand break nodes. To model the ability of the cell to
751 repair these insults, we allow these nodes to activate repair mechanisms, while also activating
752 `UrDSB` (Unrepaired DSB). If the repair mechanisms are active, as in healthy cells, this means that
753 UrDSB is inhibited by the activity of those mechanisms to represent the initial insult due to

754 radiotherapy being resolved without causing death, while any damage to the repair pathways
755 will let DSB activate UrDSB and in turn leads to death. Unrepaired SSB are modelled as leading to
756 single-ended or blunt ended DSB (seDSB and DSB) respectively but not leading to death by
757 themselves.
758 We model radio-sensitisation as the increase in death, decrease in proliferation, or decrease in
759 overall survival (proliferation - death) in the combination vs the most effective of the two possible
760 monotherapies (knock-out alone or IR alone).

761 **CRISPR knockout of radioprotective and radio-sensitising genes**

762 A CRISPR screen was performed using a pooled library across the 6 NSCLC, Cas9-expressing, lines
763 using 1Gy given twice over 24 hours (i.e., 2Gy in 2 doses over 2 days). Cells were irradiated using
764 an IBL 637 Irradiator (CS 137 gamma rays below sample). Cells were harvested from day 7 to day
765 31 (up until cells reached 10-12 doublings) and DNA was prepared for next generation
766 sequencing. Hits were identified using MAGeCK RRA (version 0.5.8). Cut-offs of FDR<0.2 and
767 FDR<0.1 were used to define significant depleted genes.
768 Due to the *in vitro* CRISPR screen considering all 20,000 human genes, when a knock-out was
769 observed to have an effect in only a subset of the cell lines it was not possible to conclude
770 whether this was due to a vulnerability contingent on a specific mutational profile, or the power
771 of the screen. For this reason, we measure and compare the number of cell lines in which a knock-
772 out was radio-sensitising in the CRISPR experiments vs the *in silico* model (i.e., recurrence).
773 A second screen was conducted with a focussed panel, across the SW1573, SW1573 *TP53*$^{-/-}$, A549
774 and A549 *TP53*$^{-/-}$ cell lines and AZSA-011N organoids. After 72 hours, we irradiated cell cultures
775 with a single fraction of 4Gy. Post-irradiation, precisely after 1 hour, 24 hours, and 48 hours,
776 irradiated and non-irradiated plates were fixed for immunofluorescence.
777

778 **Generation of organoids normal tissue organoids**

779 Patient derived lung organoids (PDO) were isolated from adjacent normal tissues from consented
780 NSCLC patients at Royal Papworth Hospital via the Royal Papworth Hospital Tissue Bank
781 application ID T02612 / East of England - Cambridge East Research Ethics Committee reference
782 18/EE/0269.
783

784 **Cell culture**

785 HCC-44-Cas9, SW1573-Cas9, H1792-Cas9, H1373-Cas9, H358-Cas9 and H23-Cas9 cell lines were
786 maintained in RPMI 1640 (Gibco) supplemented with 10% FBS (Biowest), 1% GlutaMax (Gibco)
787 and 1% pen/strep (Gibco). Cell lines were passaged every 3/4 days by dissociating to single cell
788 using Accutase (Biowest).
789

790 **Genomic DNA isolation and Next Generation Sequencing (NGS)**

791 Genomic DNA (gDNA) was isolated using the QIAamp DNA Blood Midi or Maxi Kit (Qiagen)
792 according to manufacturer's instruction. NGS libraries were prepared in a two-step process: the
793 integrated lentiviral cassette containing the gRNA was amplified from gDNA. Forward primer 5'
794 ACACTCTTTCCCTACACGACGCTCTTCCGATCTCTTGTGGAAAGGACGAAACA 3' with reverse primer

795 5'TGACTGGAGTTCAGACGTGTGCTCTTCCGATCTACCCAGACTGCTCATCGTC 3' was used for this.
796 PCR reactions with 5µg gDNA per well were set up using the Q5 Hot Start High-Fidelity 2× Master
797 Mix (NEB #M0494) in a total volume of 50µl. PCR reactions were scaled accordingly to amplify
798 the gRNAs at a coverage of at least 200-fold. The PCR products were then purified using QIAquick
799 PCR Purification Kit (Qiagen #28106). Final NGS libraries were generated using 2.5ng of the
800 purified 1st PCR product using the dual-indexing Illumina-compatible DNA HT Dual Index kit
801 (Takara #R400661). 2nd PCR products were purified with AMPure XP beads (Beckman Coulter
802 #A63881) at an 0.7 ratio. Purified 2nd step libraries were quantified using the Qubit dsDNA
803 Quantification Assay Kit (ThermoFisher) and sequenced on NovaSeq6000 by PE50bp with a 30%
804 PhiX spike-in.
805

806 **Genetic modification of p53 status of NSCLC cell lines**
807

808 The SW1573 line underwent TP53 knockout using a standard CRISPR-based knockout approach
809 to generate a polyclonal TP53 knockout population. Loss of TP53 was confirmed using PCR and
810 western blotting.
811

812 **Stratification of patient data using results from model**

813 Clinical and genomic data for lung adenocarcinoma (LUAD) and lung squamous cell carcinoma
814 (LUSC) were obtained from The Cancer Genome Atlas (TCGA) Research Network
815 (https://www.cancer.gov/tcga) and the cBioPortal platform[92,93] via the RTCGA.clinical R package.
816 Clinical data was categorized based on whether patients received radiotherapy or not, using the
817 patients not receiving radiotherapy as a positive control. Molecular data included RNA
818 expression and Capped relative linear copy-number (CN) values for each gene (from Affymetrix
819 SNP6) and was extracted via the TCGAretriever R package. To identify patients with low
820 expression or alterations in the genes of interest, the CNA and RNA datasets were combined for
821 both LUAD and LUSC. We identified patients as radiosensitive if they had gene expression or CN
822 values below specific quantile thresholds (5th percentile for CNA, 10th percentile for RNA) for at
823 least one gene in our model-defined set of radio-sensitising genes. To associate patient strata
824 with clinical outcomes we used the Cox proportional hazards regression model in R. To visualise
825 the survival probability over time as a function of the lowest CN we used the R package
826 contsurvplot[94].

827 **Statistical analysis of combination drug sensitivity**

828 For drug combination we use the dataset available from Nair *et al.* (2022) and take all the drug
829 inhibitors they used and compare them to our predictions. Nair *et al.* use HSA and so we
830 compared our value for additivity (see above). For statistical analysis, we visualise t test between
831 HSAs of different treatments for different values of additivity that the model predicts (-3 through
832 1) and compare this to treatments predicted to be not additive. Also, to factor in the ordinal
833 nature of the model's prediction, we calculate overall correlation using Kendall's tau test and bin
834 experimentally measured HSA into 4 quartiles.

835 **Linear regression to identify genetic determinants of response**

836 We separate the drug treatments into the clusters outlined above and train a linear model to
837 relate drug response (measured by additivity) with the mutational profile of the cell lines. P
838 values were adjusted for multiple hypothesis correction between each drug cluster using the
839 method devised by Benjamini & Hochberg (1995)[95].
840

841 Acknowledgments

842 This work was supported by Cancer Research UK grant C17918/A28870 (G.J.H. and J.F.), CRUK
843 Convergence Science Centre, Experimental Cancer Medicine Centre and NIHR Biomedical
844 Research Centre (L.P., U.B. and J.C.), and National Institute for Health Research University College
845 London Hospitals Biomedical Research Centre (J.F.).

846 **References**

847 1. Guo, H. *et al.* "How Long Have I Got?" in Stage IV NSCLC Patients With at Least 3 Months Up
848 to 10 Years Survival, Accuracy of Long-, Intermediate-, and Short-Term Survival Prediction Is
849 Not Good Enough to Answer This Question. *Front. Oncol.* **11**, (2021).
850 2. Li, J. & Kwok, H. F. Current Strategies for Treating NSCLC: From Biological Mechanisms to
851 Clinical Treatment. *Cancers* **12**, 1587 (2020).
852 3. Quaresma, M., Coleman, M. P. & Rachet, B. 40-year trends in an index of survival for all
853 cancers combined and survival adjusted for age and sex for each cancer in England and
854 Wales, 1971-2011: a population-based study. *Lancet Lond. Engl.* **385**, 1206–1218 (2015).
855 4. Wu, F. *et al.* Single-cell profiling of tumor heterogeneity and the microenvironment in
856 advanced non-small cell lung cancer. *Nat. Commun.* **12**, 2540 (2021).
857 5. Mok, T. S. *et al.* Gefitinib or carboplatin-paclitaxel in pulmonary adenocarcinoma. *N. Engl. J.*
858 *Med.* **361**, 947–957 (2009).
859 6. Rosell, R. *et al.* Erlotinib versus standard chemotherapy as first-line treatment for European
860 patients with advanced EGFR mutation-positive non-small-cell lung cancer (EURTAC): a
861 multicentre, open-label, randomised phase 3 trial. *Lancet Oncol.* **13**, 239–246 (2012).
862 7. Maemondo, M. *et al.* Gefitinib or chemotherapy for non-small-cell lung cancer with
863 mutated EGFR. *N. Engl. J. Med.* **362**, 2380–2388 (2010).
864 8. Mascaux, C., Tomasini, P., Greillier, L. & Barlesi, F. Personalised medicine for nonsmall cell
865 lung cancer. *Eur. Respir. Rev.* **26**, (2017).
866 9. Overview | Lung cancer: diagnosis and management | Guidance | NICE.
867 https://www.nice.org.uk/guidance/ng122 (2019).

868 10. Zhao, L. *et al.* The Determinant of DNA Repair Pathway Choices in Ionising Radiation-
869 Induced DNA Double-Strand Breaks. *BioMed Res. Int.* **2020**, 4834965 (2020).
870 11. Roos, W. P. & Kaina, B. DNA damage-induced cell death by apoptosis. *Trends Mol. Med.* **12**,
871 440–450 (2006).
872 12. Stokes, W. A. *et al.* Post-Treatment Mortality After Surgery and Stereotactic Body
873 Radiotherapy for Early-Stage Non–Small-Cell Lung Cancer. *J. Clin. Oncol.* **36**, 642–651
874 (2018).
875 13. Chi, A., Fang, W., Sun, Y. & Wen, S. Comparison of Long-term Survival of Patients With Early-
876 Stage Non-Small Cell Lung Cancer After Surgery vs Stereotactic Body Radiotherapy. *JAMA*
877 *Netw. Open* **2**, e1915724 (2019).
878 14. Aravindan, N. *et al.* Acquired tumor cell radiation resistance at the treatment site is
879 mediated through radiation-orchestrated intercellular communication. *Int. J. Radiat. Oncol.*
880 *Biol. Phys.* **88**, 677–685 (2014).
881 15. Chuang, R. *et al.* Drug Target Optimization in Chronic Myeloid Leukemia Using Innovative
882 Computational Platform. *Sci. Rep.* **5**, 8190 (2015).
883 16. Clarke, M. A., Woodhouse, S., Piterman, N., Hall, B. A. & Fisher, J. Using State Space
884 Exploration to Determine How Gene Regulatory Networks Constrain Mutation Order in
885 Cancer Evolution. in *Automated Reasoning for Systems Biology and Medicine* (eds. Liò, P. &
886 Zuliani, P.) 133–153 (Springer International Publishing, Cham, 2019). doi:10.1007/978-3-
887 030-17297-8_5.
888 17. Clarke, M. A. & Fisher, J. Executable cancer models: successes and challenges. *Nat. Rev.*
889 *Cancer* **20**, 343–354 (2020).

890 18. Howell, R. *et al.* Localized immune surveillance of primary melanoma in the skin deciphered
891 through executable modeling. *Sci. Adv.* **9**, eadd1992 (2023).
892 19. Kreuzaler, P. *et al.* Heterogeneity of Myc expression in breast cancer exposes
893 pharmacological vulnerabilities revealed through executable mechanistic modeling. *Proc.*
894 *Natl. Acad. Sci.* **116**, 22399–22408 (2019).
895 20. Silverbush, D. *et al.* Cell-Specific Computational Modeling of the PIM Pathway in Acute
896 Myeloid Leukemia. *Cancer Res.* **77**, 827–838 (2017).
897 21. Talarmain, L. *et al.* HOXA9 has the hallmarks of a biological switch with implications in blood
898 cancers. *Nat. Commun.* **13**, 5829 (2022).
899 22. Schaub, M. A., Henzinger, T. A. & Fisher, J. Qualitative networks: a symbolic approach to
900 analyze biological signaling networks. *BMC Syst. Biol.* **1**, 4 (2007).
901 23. Fisher, J. & Henzinger, T. A. Executable cell biology. *Nat. Biotechnol.* **25**, 1239–1249 (2007).
902 24. Chevallier, M., Borgeaud, M., Addeo, A. & Friedlaender, A. Oncogenic driver mutations in
903 non-small cell lung cancer: Past, present and future. *World J. Clin. Oncol.* **12**, 217–237
904 (2021).
905 25. van der Meer, D. *et al.* Cell Model Passports-a hub for clinical, genetic and functional
906 datasets of preclinical cancer models. *Nucleic Acids Res.* **47**, D923–D929 (2019).
907 26. Gao, J. *et al.* A novel epidermal growth factor receptor inhibitor for treating lung cancer.
908 *Tumour Biol. J. Int. Soc. Oncodevelopmental Biol. Med.* **39**, 1010428317698358 (2017).
909 27. Li, J. *et al.* Inhibition of non-small cell lung cancer (NSCLC) growth by a novel small
910 molecular inhibitor of EGFR. *Oncotarget* **6**, 6749–6761 (2015).

911 28. Chiba, M. *et al.* MEK inhibitors against MET-amplified non-small cell lung cancer. *Int. J.*
912 *Oncol.* **49**, 2236–2244 (2016).
913 29. Fok, J. H. L. *et al.* AZD7648 is a potent and selective DNA-PK inhibitor that enhances
914 radiation, chemotherapy and olaparib activity. *Nat. Commun.* **10**, 5065 (2019).
915 30. Yang, L. *et al.* Inhibition of DNA-PK activity sensitizes A549 cells to X-ray irradiation by
916 inducing the ATM-dependent DNA damage response. *Mol. Med. Rep.* **17**, 7545–7552
917 (2018).
918 31. Minjgee, M., Toulany, M., Kehlbach, R., Giehl, K. & Rodemann, H. P. K-RAS(V12) induces
919 autocrine production of EGFR ligands and mediates radioresistance through EGFR-
920 dependent Akt signaling and activation of DNA-PKcs. *Int. J. Radiat. Oncol. Biol. Phys.* **81**,
921 1506–1514 (2011).
922 32. Sato, M., Shay, J. W. & Minna, J. D. Immortalized normal human lung epithelial cell models
923 for studying lung cancer biology. *Respir. Investig.* **58**, 344–354 (2020).
924 33. Wang, M. *et al.* Radiation Resistance in KRAS-Mutated Lung Cancer Is Enabled by Stem-like
925 Properties Mediated by an Osteopontin-EGFR Pathway. *Cancer Res.* **77**, 2018–2028 (2017).
926 34. Singhal, A., Li, B. T. & O'Reilly, E. M. Targeting KRAS in cancer. *Nat. Med.* **30**, 969–983
927 (2024).
928 35. Xu, T. *et al.* MUC1 downregulation inhibits non-small cell lung cancer progression in human
929 cell lines. *Exp. Ther. Med.* **14**, 4443–4447 (2017).
930 36. Homma, S. *et al.* Nrf2 enhances cell proliferation and resistance to anticancer drugs in
931 human lung cancer. *Clin. Cancer Res. Off. J. Am. Assoc. Cancer Res.* **15**, 3423–3432 (2009).

932 37. Wang, X.-J. *et al.* Nrf2 enhances resistance of cancer cells to chemotherapeutic drugs, the
933 dark side of Nrf2. *Carcinogenesis* **29**, 1235–1243 (2008).
934 38. Xu, Y., Jin, J., Xu, J., Shao, Y. W. & Fan, Y. JAK2 variations and functions in lung
935 adenocarcinoma. *Tumour Biol. J. Int. Soc. Oncodevelopmental Biol. Med.* **39**,
936 1010428317711140 (2017).
937 39. Cortez, M. A. *et al.* In Vivo Delivery of miR-34a Sensitizes Lung Tumors to Radiation Through
938 RAD51 Regulation. *Mol. Ther. Nucleic Acids* **4**, e270 (2015).
939 40. Di Francesco, A. *et al.* The DNA-damage response to γ-radiation is affected by miR-27a in
940 A549 cells. *Int. J. Mol. Sci.* **14**, 17881–17896 (2013).
941 41. Zhou, H. *et al.* RNAi silencing targeting RNF8 enhances radiosensitivity of a non-small cell
942 lung cancer cell line A549. *Int. J. Radiat. Biol.* **89**, 708–715 (2013).
943 42. Wael, H. *et al.* Notch1 signaling controls cell proliferation, apoptosis and differentiation in
944 lung carcinoma. *Lung Cancer Amst. Neth.* **85**, 131–140 (2014).
945 43. Edelmann, M. *et al.* Cell cycle effects of radiation on human bronchial epithelium and lung
946 carcinoma cells in monolayer cultures and a three-dimensional co-culture system. *Radiat.*
947 *Res.* **164**, 391–399 (2005).
948 44. Caldecott, K. W. Causes and consequences of DNA single-strand breaks. *Trends Biochem.*
949 *Sci.* **49**, 68–78 (2024).
950 45. Liao, H., Ji, F., Helleday, T. & Ying, S. Mechanisms for stalled replication fork stabilization:
951 new targets for synthetic lethality strategies in cancer treatments. *EMBO Rep.* **19**, e46263
952 (2018).

953 46. Balmus, G. *et al.* ATM orchestrates the DNA-damage response to counter toxic non-
954 homologous end-joining at broken replication forks. *Nat. Commun.* **10**, 87 (2019).
955 47. Takahashi, A. *et al.* Nonhomologous End-Joining Repair Plays a More Important Role than
956 Homologous Recombination Repair in Defining Radiosensitivity after Exposure to High-LET
957 Radiation. *Radiat. Res.* **182**, 338–344 (2014).
958 48. Kühne, M. *et al.* A Double-Strand Break Repair Defect in ATM-Deficient Cells Contributes to
959 Radiosensitivity. *Cancer Res.* **64**, 500–508 (2004).
960 49. Evan, G. & Littlewood, T. A Matter of Life and Cell Death. *Science* **281**, 1317–1322 (1998).
961 50. Williams, T. M., Yang, L., Estrada-Bernal, A., Chatterjee, M. & Robb, R. A KRAS-NRF2-53BP1
962 Nonhomologous End-Joining Repair Pathway Mediates Oncogenic KRAS Radioresistance.
963 *Int. J. Radiat. Oncol. Biol. Phys.* **99**, S31 (2017).
964 51. Larkin, J. *et al.* Combined Nivolumab and Ipilimumab or Monotherapy in Untreated
965 Melanoma. *N. Engl. J. Med.* **373**, 23–34 (2015).
966 52. Bozic, I. *et al.* Evolutionary dynamics of cancer in response to targeted combination
967 therapy. *eLife* **2**, e00747 (2013).
968 53. Baskar, R., Lee, K. A., Yeo, R. & Yeoh, K.-W. Cancer and Radiation Therapy: Current
969 Advances and Future Directions. *Int. J. Med. Sci.* **9**, 193–199 (2012).
970 54. Nair, N. U. *et al.* A landscape of response to drug combinations in non-small cell lung
971 cancer. *Nat. Commun.* **14**, 3830 (2023).
972 55. Yang, W. *et al.* Genomics of Drug Sensitivity in Cancer (GDSC): a resource for therapeutic
973 biomarker discovery in cancer cells. *Nucleic Acids Res.* **41**, D955-961 (2013).

974 56. Seashore-Ludlow, B. *et al.* Harnessing Connectivity in a Large-Scale Small-Molecule
975 Sensitivity Dataset. *Cancer Discov.* **5**, 1210–1223 (2015).
976 57. Corsello, S. M. *et al.* Discovering the anticancer potential of non-oncology drugs by
977 systematic viability profiling. *Nat. Cancer* **1**, 235–248 (2020).
978 58. Sinha, S. *et al.* PERCEPTION predicts patient response and resistance to treatment using
979 single-cell transcriptomics of their tumors. *Nat. Cancer* 1–15 (2024) doi:10.1038/s43018-
980 024-00756-7.
981 59. Beaulieu, M.-E. *et al.* Intrinsic cell-penetrating activity propels Omomyc from proof of
982 concept to viable anti-MYC therapy. *Sci. Transl. Med.* **11**, eaar5012 (2019).
983 60. Llombart, V. & Mansour, M. R. Therapeutic targeting of 'undruggable' MYC. *EBioMedicine*
984 **75**, 103756 (2022).
985 61. Peptomyc S.L. *A Phase 1/2 Study to Evaluate the Safety, Pharmacokinetics, and Anti-Tumour*
986 *Activity of the MYC Inhibitor OMO-103 Administered Intravenously in Patients With*
987 *Advanced Solid Tumours*. https://clinicaltrials.gov/study/NCT04808362 (2022).
988 62. Coker, E. A. *et al.* Individualized Prediction of Drug Response and Rational Combination
989 Therapy in NSCLC Using Artificial Intelligence–Enabled Studies of Acute Phosphoproteomic
990 Changes. *Mol. Cancer Ther.* **21**, 1020–1029 (2022).
991 63. Tolcher, A. W., Peng, W. & Calvo, E. Rational Approaches for Combination Therapy
992 Strategies Targeting the MAP Kinase Pathway in Solid Tumors. *Mol. Cancer Ther.* **17**, 3–16
993 (2018).
994 64. Poole, C. J. & van Riggelen, J. MYC—Master Regulator of the Cancer Epigenome and
995 Transcriptome. *Genes* **8**, 142 (2017).

996 65. Gabay, M., Li, Y. & Felsher, D. W. MYC Activation Is a Hallmark of Cancer Initiation and
997 Maintenance. *Cold Spring Harb. Perspect. Med.* **4**, (2014).
998 66. Soucek, L. *et al.* Inhibition of Myc family proteins eradicates KRas-driven lung cancer in
999 mice. *Genes Dev.* **27**, 504–513 (2013).
1000 67. Savino, M. *et al.* The action mechanism of the Myc inhibitor termed Omomyc may give
1001 clues on how to target Myc for cancer therapy. *PloS One* **6**, e22284 (2011).
1002 68. Wang, C. *et al.* Alternative approaches to target Myc for cancer treatment. *Signal*
1003 *Transduct. Target. Ther.* **6**, 1–14 (2021).
1004 69. Garralda, E. *et al.* MYC targeting by OMO-103 in solid tumors: a phase 1 trial. *Nat. Med.* **30**,
1005 762–771 (2024).
1006 70. Luoto, K. R. *et al.* Tumor cell kill by c-MYC depletion: role of MYC-regulated genes that
1007 control DNA double-strand break repair. *Cancer Res.* **70**, 8748–8759 (2010).
1008 71. Vokes, N. I. *et al.* Concurrent TP53 Mutations Facilitate Resistance Evolution in EGFR-
1009 Mutant Lung Adenocarcinoma. *J. Thorac. Oncol.* **17**, 779–792 (2022).
1010 72. Hobor, S. *et al.* Mixed responses to targeted therapy driven by chromosomal instability
1011 through p53 dysfunction and genome doubling. *Nat. Commun.* **15**, 4871 (2024).
1012 73. Cheng, G. *et al.* The tumor suppressor, p53, contributes to radiosensitivity of lung cancer
1013 cells by regulating autophagy and apoptosis. *Cancer Biother. Radiopharm.* **28**, 153–159
1014 (2013).
1015 74. Gudkov, A. V. & Komarova, E. A. Pathologies Associated with the p53 Response. *Cold Spring*
1016 *Harb. Perspect. Biol.* **2**, a001180 (2010).

1017 75. Lee, C.-L., Blum, J. M. & Kirsch, D. G. Role of p53 in regulating tissue response to radiation
1018 by mechanisms independent of apoptosis. *Transl. Cancer Res.* **2**, 412–421 (2013).
1019 76. Stewart-Ornstein, J. *et al.* p53 dynamics vary between tissues and are linked with radiation
1020 sensitivity. *Nat. Commun.* **12**, 898 (2021).
1021 77. Zhang, J., Shen, L. & Sun, L.-Q. The regulation of radiosensitivity by p53 and its acetylation.
1022 *Cancer Lett.* **363**, 108–118 (2015).
1023 78. Hao, F., Gu, L. & Zhong, D. TP53 Mutation Mapping in Advanced Non-Small Cell Lung
1024 Cancer: A Real-World Retrospective Cohort Study. *Curr. Oncol.* **29**, 7411–7419 (2022).
1025 79. Chang, Y.-L., Wu, C.-T., Shih, J.-Y. & Lee, Y.-C. Comparison of p53 and epidermal growth
1026 factor receptor gene status between primary tumors and lymph node metastases in non-
1027 small cell lung cancers. *Ann. Surg. Oncol.* **18**, 543–550 (2011).
1028 80. Steeg, P. S. Tumor metastasis: mechanistic insights and clinical challenges. *Nat. Med.* **12**,
1029 895–904 (2006).
1030 81. Walls, G. M. *et al.* CONCORDE: A phase I platform study of novel agents in combination with
1031 conventional radiotherapy in non-small-cell lung cancer. *Clin. Transl. Radiat. Oncol.* **25**, 61–
1032 66 (2020).
1033 82. Dharia, N. V. *et al.* A first-generation pediatric cancer dependency map. *Nat. Genet.* **53**,
1034 529–538 (2021).
1035 83. Jaaks, P. *et al.* Effective drug combinations in breast, colon and pancreatic cancer cells.
1036 *Nature* **603**, 166–173 (2022).
1037 84. Guo, C., Ma, X., Gao, F. & Guo, Y. Off-target effects in CRISPR/Cas9 gene editing. *Front.*
1038 *Bioeng. Biotechnol.* **11**, 1143157 (2023).

1039 85. Sheel, A. & Xue, W. Genomic amplifications cause false positives in CRISPR screens. *Cancer*
1040 *Discov.* **6**, 824–826 (2016).
1041 86. Dede, M. & Hart, T. Recovering false negatives in CRISPR fitness screens with JLOE. *Nucleic*
1042 *Acids Res.* **51**, 1637–1651 (2023).
1043 87. Eduati, F. *et al.* Patient-specific logic models of signaling pathways from screenings on
1044 cancer biopsies to prioritize personalized combination therapies. *Mol. Syst. Biol.* **16**, e8664
1045 (2020).
1046 88. Fröhlich, F. *et al.* Efficient Parameter Estimation Enables the Prediction of Drug Response
1047 Using a Mechanistic Pan-Cancer Pathway Model. *Cell Syst.* **7**, 567-579.e6 (2018).
1048 89. Fong, S. H. *et al.* A multilineage screen identifies actionable synthetic lethal interactions in
1049 human cancers. *Nat. Genet.* 1–11 (2024) doi:10.1038/s41588-024-01971-9.
1050 90. Cook, B., Fisher, J., Krepska, E. & Piterman, N. Proving Stabilization of Biological Systems. in
1051 *Verification, Model Checking, and Abstract Interpretation* (eds. Jhala, R. & Schmidt, D.) 134–
1052 149 (Springer, Berlin, Heidelberg, 2011). doi:10.1007/978-3-642-18275-4_11.
1053 91. Zhu, Q. *et al.* Single cell multi-omics reveal intra-cell-line heterogeneity across human
1054 cancer cell lines. *Nat. Commun.* **14**, 8170 (2023).
1055 92. de Bruijn, I. *et al.* Analysis and Visualization of Longitudinal Genomic and Clinical Data from
1056 the AACR Project GENIE Biopharma Collaborative in cBioPortal. *Cancer Res.* **83**, 3861–3867
1057 (2023).
1058 93. Yard, B. D. *et al.* A genetic basis for the variation in the vulnerability of cancer to DNA
1059 damage. *Nat. Commun.* **7**, 11428 (2016).

1060 94. Denz, R. & Timmesfeld, N. Visualizing the (Causal) Effect of a Continuous Variable on a
1061 Time-To-Event Outcome. *Epidemiol. Camb. Mass* **34**, 652–660 (2023).
1062 95. Benjamini, Y. & Hochberg, Y. Controlling the False Discovery Rate: A Practical and Powerful
1063 Approach to Multiple Testing. *J. R. Stat. Soc. Ser. B Methodol.* **57**, 289–300 (1995).
1064 96. Abbosh, C. *et al.* Phylogenetic ctDNA analysis depicts early-stage lung cancer evolution.
1065 *Nature* **545**, 446–451 (2017).
1066 97. Jamal-Hanjani, M. *et al.* Tracking the Evolution of Non-Small-Cell Lung Cancer. *N. Engl. J.*
1067 *Med.* **376**, 2109–2121 (2017).
1068
1069

1070 # Supplementary Information

1071 ## Supplementary Notes

1072

1073 To assess the predictions of the model, we compared our predictions of Additivity to those observed by
1074 Nair *et al*, which were not used to train the model. As of writing, MYC inhibitors are in early stage trials[47–
1075 49], however, other specific drug combinations that we predict to be additive are also tested in Nair *et al.*
1076 Here, we illustrate how the model can predict differential cell line sensitivities for the most effective drugs.
1077 Additive score, as predicted with the model, had a positive correlation with the HSA results of Nair *et al.*
1078 in 5 cases (Supplementary Figure S7A). We observe positive correlation between predicted additive score
1079 and HSA in all but one of the drug combinations (inhibition of AKT+MEK, EGFR+PI3K, JAK2+MET and
1080 EGFR/Erbb1+MET). This illustrates how the model can predict differential cell line sensitivities for the most
1081 effective drugs. JAK2+PI3K is the drug combination where the model prediction does not align with the
1082 experimental predictions. However, of these 6 combinations, JAK2+PI3K inhibition has the highest
1083 variance in Nair *et al.*'s results (Supplementary figure S7B) Nair *et al.*'s experimental results for additivity
1084 for JAK2 inhibition and PI3K inhibition are highly dependent on the specific drugs used to target either
1085 JAK2 or PI3K, for example drug Fedratinib and AT9283 have very different effects, despite both being
1086 inhibitors of JAK2, and as such the results are likely to be because of off-target effects of the drugs rather
1087 than through the direct inhibition of JAK2 or PI3K[50,69].

1088

1089 The model predicts AKT+MEK inhibition to be broadly effective across cancer cell lines. Indeed, it is a
1090 combination that is often used as a positive control for synergy experiments. The experimental data
1091 affirms this, aside from the cell line HCC827, which is predicted to be maximally additive (-3) but displays
1092 no additive inhibition in experimental data. This discrepancy conflicts with the similarity of mutational
1093 information for PC9 and HCC827, with both having oncogenic mutations in Erbb1 and p53 (Supplementary
1094 Figure S7G). Another study, Coker *et al.,* measured synergy between these two drugs in HCC827 found
1095 strong synergy (Bliss score of 0.6, Supplementary Figure S7B)[51], implying high additivity also and thus
1096 agreeing with our predictions. From this we hypothesise that likely the strain of HCC827 that Nair *et al.* is
1097 using likely contains some uncharacterised differences that disrupt this synergy, otherwise it would
1098 behave similarly to PC9 as the simulations would suggest and as seen in Coker *et al*. In EGFR+PI3K
1099 combined drug inhibition we see the same discrepancy. Although we see correlation, this combination
1100 displays less additivity in HCC827 than our predictions would suggest. The consistent effects with both
1101 HCC827 and NCIH1792 suggest similarly that there are unknown mutations or amplifications within these
1102 cell lines causing additivity in ways that our model cannot predict[54,62].

1103

1104 The model correctly predicts additivity of MET inhibition with either JAK2 inhibition or EGFR/Erbb1
1105 inhibition in NCIH1993. Predictions indicate this is because the MET receptor is amplified in NCIH1993,
1106 which drives oncogenic signalling primarily along down MAPK and AKT pathways, but JAK2 is still active.
1107 EGFR/Erbb1 is also able to activate JAK/STAT signalling and so combined inhibition of either of these
1108 proteins can produce an additive effect (Supplementary Figure S7G). Despite broad concordance between
1109 model and data, SW1573 appears to display some marginal additivity in the experimental data despite
1110 the model predicting it not to be additive (Supplementary Figure S7D). This cell line is characterised as
1111 having its oncogenic mutations in both PI3K and RAS, both downstream of MET (Figure 6G) and so the
1112 model does not predict an additive behaviour by targeting MET or JAK2. The experimental data from Nair
1113 *et al.* would suggest that MET plays a role in this cell line either in the response to inhibition of JAK2 or in
1114 that it is amplified in this cell line in a way that is uncharacterised.

1115 **List of Supplementary Figures**

1116

1117 **Figure S1.** Schematic showing the mutations used to model cell lines. **A)** The schematic (right) shows
1118 mutations as columns and cell lines as rows, with gain- of-function mutations for a cell line and loss-of-
1119 function (grey). **B)** Schematic showing the presence of these mutations across clinical data (Plotted using
1120 cBio-Portal, using studies from TRACERx[96,97]).
1121

1122 **Figure S2.** Heatmap showing the simulation of the model after perturbation with single drug treatments.
1123 The columns are various cancer cell lines with healthy cells at the far left. Rows indicate druggable proteins
1124 that are included in the model. Values in the model correspond to proliferation (**A**, in green), death (**B**, in
1125 red) and the difference between proliferation and death (**C**, red to blue). For the difference between them,
1126 positive values (blue) indicate growth and negative values (red) indicate death. The baseline values for
1127 cell lines (readings without any perturbation) are shown on the bottom of the heatmaps).

1128 **Figure S3. A)** Schematic showing the part of the model that models irradiation and DNA-damage repair.
1129 **B-C)** Predicted cell death and therapeutic window (difference in death between cancer and healthy
1130 cells). Effect of gene knockouts (rows) on different cell line backgrounds (columns). Colour represents the
1131 activity of the node, side panels (green) show recurrence i.e. the number of cell line backgrounds in which
1132 the treatment was radio-sensitising in the model or the CRISPR screen (at FDR ≤ 0.2 and < 0.1): cell death
1133 **(B)** and therapeutic window **(C)** difference between radiotherapy and knockout in cell line compared to
1134 WT cells). Purple boxes indicate knockouts of particular interest. **D)** CRISPR results. **E)** Scatter plots
1135 showing the difference in DNA-damage associated radiosensitivity in cancer (y axis) versus healthy cells (x
1136 axis). Black is more radio-sensitisation of cancer than healthy, yellow is more radio-sensitisation of healthy
1137 than cancer. Point size is the number of knockouts that have this effect.

1138 **Figure S4. A)** p53 experimental results. **B)** Level of cell death (x-axis) in each cell line for each simulated
1139 knock-out in combination with IR (y-axis) comparing the effect in a p53-competent (blue) or a p53-
1140 deficient (red) version of that cell line. **C)** Number of simulated knockouts leading to each possible level
1141 of cell death for p53-competent (blue) and p53-deficient (red) cell lines. **D)** Density plot of number of
1142 simulated knockouts leading to each possible level of cell death for p53-competent (blue) and p53-
1143 deficient (red) cell lines

1144 **Figure S5. A)** Plot illustrating TCGA data of radiation treated patients (columns) according to the basal
1145 activity of predicted radio-sensitising genes (rows). Cells indicate the presence of low levels of CNV
1146 (yellow) or expression (black) for a particular gene. The predicted radiosensitivity of the patients is marked
1147 blue (sensitive) or red (resistant) by the bars on the top. Also shown is the minimum RNA expression and
1148 CNV levels for each patient and histograms showing the frequency of alterations for each patient (top)
1149 and gene (left). **B, C)** *In silico* predictions stratify radiation-treated patients into radiosensitive and
1150 radioresistant strata. Kaplan-Meier survival curves showing the differences in survival (days) between
1151 radioresistant patients (red) and radiosensitive patients (blue) for patients treated with radiation. These
1152 patients were stratified based on their expression levels (B) or their copy-number levels (C). **D)** Plot
1153 illustrating TCGA data of patients not treated with radiotherapy (columns) according to the basal activity
1154 of predicted radio-sensitising genes (rows). Cells indicate the presence of low levels of CNV (yellow) or
1155 expression (black) for a particular gene. The predicted radiosensitivity of the patients is marked blue
1156 (sensitive) or red (resistant) by the bars on the top. Also shown is the minimum RNA expression and CNV
1157 levels for each patient and histograms showing the frequency of alterations for each patient (top) and
1158 gene (left). **E, F)** Kaplan-Meier survival curves showing the differences in survival (days) between predicted

radioresistant patients (red) and radiosensitive patients (blue) for patients treated without radiotherapy. These patients were predicted radioresistant according to expression levels (E) or copy number levels (F). The x-axis indicates the time since diagnosis and y-axis indicates the survival probability (days). **G)** Kaplan-Meier survival curves showing the differences in survival (days) between predicted radioresistant (according to consensus expression and copy number levels) patients (red) and radiosensitive patients (blue) for patients treated without radiation.

Figure S6. Circular heatmaps showing the effect of drug combinations on selected NSCLC cell lines. Columns (spokes of the wheel) are the drug combinations. **A)** Heatmap showing additivity. A darker red colour indicates those combinations that have a greater additive effect, while blue represents those drugs with antagonistic effects (the drugs cancel one another out). The plot in the inner wheel of the circle shows the mean additive effect of a drug across all cell lines and is red for those drug combinations with overall additive effect and blue for those antagonise each other. **B)** Heatmap showing death (in red, inner circle) and proliferation (in green, outer circle). Darker colours indicate higher values for the phenotypes.

Figure S7. Concordance of simulated results for drug combinations with Nair *et al.* **A)** Violin plot showing the additive score as predicted by the model (x axis, see Methods) versus the HSA measured experimentally by Nair *et al.* (y axis). Significance is illustrated through dotted lines from those drug combinations that are not predicted to be additive. **B)** Visualisation of predicted additivity (x axis) of drug combinations versus experimentally measured HSA (y axis) for each drug cluster. **C)** Same visualisation as panel A, but broken down by cell lines tested by Nair *et al.*

Figure S8. Concordance of simulated results with published results for individual drugs. A) Experimentally measured additivity (on the y-axis, HSA from Nair et al.) compared with the computational predicted value (x-axis) for Akt + MEK inhibition **(A)**, EGFR + PI3K inhibition **(B)**, JAK2 + PI3K inhibition **(C)**, JAK2 + MET inhibition **(D)**, EGFR + MET inhibition **(E)** and Erbb1 + MET inhibition **(F)**. The names of the drugs used are labelled on the points and the colours refers to the cell line with which the reading was taken. **G)** Subnetwork of the model illustrating the mutations in the cell lines affecting growth pathways and the regulatory interactions between them. Edges represent regulatory interactions with a pointed arrowhead referring to an activating interaction and a blunt arrowhead indicating inhibitory interactions. Coloured circles indicate where a cell line has a gain-of-function mutation, and square circles indicate where they have a low-of-function mutation. **H)** Boxplot illustrating the standard deviation of additivity (y axis) of different drugs targeting specific proteins (x axis), taken from Nair et al. **I)** Plot comparing the predicted additivity of the model for MAPK+AKT inhibition (x axis) with BLISS score (y axis), taken from Coker et al. The lower the BLISS score, the more synergistic the drug treatment is.

Figure S9. Mechanistic analysis of combined ATR and MYC inhibition. **A)** Subnetwork of the model, covering the proteins and variables that changed after treatment of MYC/ATR inhibitors in A549. Colour of the node illustrates the difference between ATR/MYC inhibition vs untreated (blue for a relative decrease in activation and red for an increase) in PC9 (outer circle) and the difference in healthy lung cells (inner circle). **B)** Subnetwork of the model, covering the proteins and variables that changed after treatment of MYC/ATR inhibitors in H1993. **C)** Mechanistic analysis of combined ATR and MYC inhibition. Subnetwork of the model, covering the proteins and variables that changed after treatment of MYC/ATR inhibitors in HCC827. **D)** Mechanistic analysis of combined ATR and MYC inhibition. Subnetwork of the model, covering the proteins and variables that changed after treatment of MYC/ATR inhibitors in NCIH1792. **E)** Mechanistic analysis of combined ATR and MYC inhibition. Subnetwork of the model, covering the proteins and variables that changed after treatment of MYC/ATR inhibitors in SW1573.

List of Supplementary Tables

Supplementary Table S1. Regulatory edges in the *in silico* model.

Supplementary Table S2. Target functions used in the network model.

Supplementary Table S3. Summary of the nodes included in the model.

Supplementary Table S4. List of mutations used to model cell lines.

Supplementary Table S5. Experiments from the literature used to validate the *in silico* model.

Supplementary Table S6. List of druggable nodes in the model and the drugs that target them.

Supplementary Table S7. List of drugs used in Nair et al. and their corresponding model targets.